

AD/A 013 731

ESD ACCESSION LIST

XRRRI Call No. 83060

Copy No. 1 of 2 cys.

FILE COPY

Technical Note

1975-28

Ionospheric Limitations
on Radar Accuracy at L-Band

R. H. Wand

27 May 1975

Prepared for the Ballistic Missile Defense Program Office,
Department of the Army,
under Electronic Systems Division Contract F19628-73-C-0002 by

Lincoln Laboratory

MASSACHUSETTS INSTITUTE OF TECHNOLOGY

LEXINGTON, MASSACHUSETTS



Approved for public release; distribution unlimited.

ADA 013731

ESD-TR 75-175
AD/A013 731

MASSACHUSETTS INSTITUTE OF TECHNOLOGY
LINCOLN LABORATORY

IONOSPHERIC LIMITATIONS ON RADAR ACCURACY AT L-BAND

R. H. WAND

Group 21

TECHNICAL NOTE 1975-28

27 MAY 1975

Approved for public release; distribution unlimited.

LEXINGTON

MASSACHUSETTS

ABSTRACT

For a long-range radar system the target range and bearing, as well as the signal amplitude and phase, are altered to some degree by the presence of the earth's atmosphere and ionosphere. The irregular nature of the ionosphere controls the extent to which these errors can be predicted and compensated for. The limits on radar metric accuracy imposed by ionospheric propagation effects are evaluated with emphasis on an L-band radar situated near the auroral zone. Many of the results are derived from previous propagation studies conducted at the Millstone Hill radar facility by applying appropriate frequency scaling laws. Estimates are made of elevation and range errors associated with the ambient ionosphere and with large-scale ionospheric structures (such as the mid-latitude electron density trough and traveling ionospheric disturbances). The amplitude and angle-of-arrival fluctuations produced by ionospheric scintillation are considered and models constructed which are applicable for normal ionospheric conditions and also for periods of severe geomagnetic disturbance.

Contents

Abstract	iii
I. <u>Introduction</u>	1
II. <u>The Millstone Hill Propagation Study</u>	4
A) General	4
B) Scintillation Study	4
C) Differential-Doppler Experiment	7
D) Refraction Measurements	8
III. <u>Elevation Errors Produced by the Ambient Ionosphere</u>	8
IV. <u>Range Errors in the Ambient Ionosphere</u>	17
V. <u>High-Latitude Effects</u>	29
A) Auroral Clutter	29
B) Electron Density Trough	30
VI. <u>TID-Induced Errors</u>	37
VII. <u>Ionospheric Scintillation</u>	47
A) General	47
B) Elevation Angle Dependence of Scintillation	51
C) Dependence on Geomagnetic Activity and Season	52
D) Scintillation Boundary	54
E) Model for Scintillation Index	60
F) Model for RMS Amplitude Fluctuations	62
G) Probability Distribution of Amplitude	63
H) Allowance for Radar Case	63
I) Correlation Time of Amplitude Fluctuations	63
J) Model for Angle Fluctuations	64
K) Model for Severe Ionospheric Scintillation	69
L) Summary of Scintillation Model	70
M) Depolarization	70
VIII. <u>Summary</u>	74
References	76

I. INTRODUCTION

This report reviews the limitations which the ionosphere imposes on the accuracy of radar measurements, with emphasis on an L-band radar (1000 MHz) operating in or near the auroral zone. The effect of the troposphere on the apparent elevation and range of a target at low elevation angles is well known and standard corrections are applied to allow for it. Ionospheric effects on radar propagation are often ignored because the necessary corrections are not as readily applied as for the troposphere. Also, a rapid decrease in the importance of ionospheric errors may be effected by increasing the operating frequency of the radar. In some applications however, the ultimate accuracy of a radar is required and all bias errors must be evaluated if possible.

The ionosphere is defined as that part of the upper atmosphere which is sufficiently ionized to influence the propagation of radiowaves, and as such extends from an altitude of 50 km to several earth radii. While many properties of this region are still not understood, the propagation of radiowaves is governed solely by the distribution of electrons along the propagation path. Examples of the vertical distribution of ionization are given in Figure 1 for typical daytime and nighttime conditions at sunspot maximum.

In practice, the propagation effects produced by the ionosphere are difficult to predict because of the large daily, seasonal, sunspot-cycle, geomagnetic activity and latitudinal variations in the ambient electron density. An additional source of propagation errors arises from the presence of inhomogeneities in the ionosphere. These inhomogeneities have a variety of scales ranging from global down to cm sizes.

Many of the results reported here were based on propagation measurements made at Millstone Hill. These measurements were made at UHF and VHF and have been scaled to L-band for the present study. However, the frequency scaling laws are given, and with some restrictions, the results could readily be scaled to other radar frequencies. A brief description of the Millstone Hill propagation study is given in Section II.

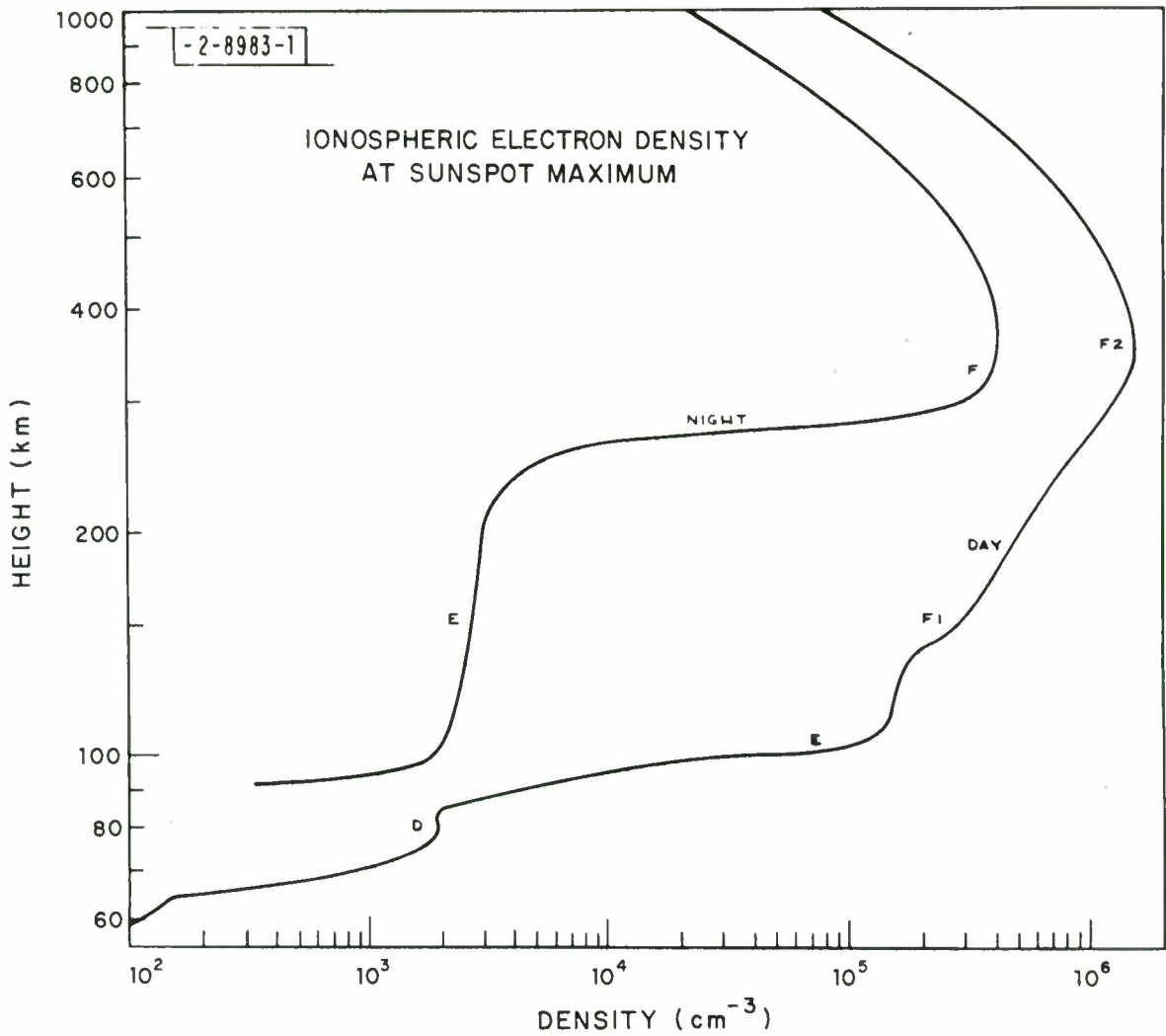


Fig. 1 An idealized electron density distribution in the earth's ionosphere. The curves drawn indicate the densities to be expected at sunspot maximum in temperate latitudes.

For the purpose of this report, the ionosphere is considered as a superposition of two components; an ambient unperturbed part and an irregular part comprising inhomogeneities of various sizes. The ambient ionosphere is assumed to be spherically symmetric in the vicinity of the radar and the resulting bias errors in elevation and range are discussed in Sections III and IV. The propagation effects produced by various types of ionospheric inhomogeneities are then discussed commencing with the largest scale phenomenon. Section V treats radar errors at high latitude which are associated with the mid-latitude trough in electron density and Section VI examines the effects produced by traveling ionospheric disturbances. Sunrise and sunset effects are usually negligible and are ignored in the present study. The effects of scintillations are treated in Section VII and a summary of the magnitude of the various propagation errors at L-band is given in the final section.

II. THE MILLSTONE HILL PROPAGATION STUDY

A. General

Many of the results presented in this report are based on a propagation study conducted from 1969 through 1973 at the Millstone Hill Radar Facility (42.6°N, 71.5°W) jointly by the staff of Lincoln Laboratory and Bell Telephone Laboratories¹. The study was supported by the U.S. Army Advanced Ballistic Missile Defense Agency (ABMDA) and the U.S. Army SAFEGUARD System Command.

During the period January 1971 to March 1973, five satellites of the Navy Navigation System were tracked with a passive multi-lobe UHF beacon tracker on the 84-foot fully-steerable antenna. A frequency selective sub-reflector was mounted in the antenna and this allowed simultaneous active tracking of the satellites with the L-band radar. The satellite beacon signal at VHF (150 MHz) was also measured with a yagi antenna mounted on the edge of the dish and combined with the phase-locked UHF (400 MHz) signal to determine differential-doppler. In addition to the satellite tracking program, regular incoherent scatter soundings were made to study the ionosphere.

A number of scintillation and refraction studies were undertaken using the tracking data and a brief outline of the various investigations which are relevant to the present work is given here.

B. Scintillation Study

The Navy Navigation satellites were in almost circular polar orbits at heights near 1100 km, and were seen rising or setting through the auroral zone to the north where scintillation effects are often observed. A total of 2376 satellite tracks were made during the measurement period, representing almost 600 hours of observations. The raw data from each track were recorded on magnetic tape as digital samples of various parameters every 1/15 sec.

The UHF beacon tracker determined the signal amplitude and the traverse (traverse = azimuth x cosine of elevation) and elevation angles. A parameter which measured the amount of fluctuation produced by ionospheric

scintillation over a three-second interval was calculated for each of these three variables.

The parameter used to characterize the UHF amplitude fluctuations was the scintillation index S , defined as the rms power about the mean divided by the mean power

$$S^2 = \frac{\langle A^4 \rangle - \langle A^2 \rangle^2}{\langle A^2 \rangle^2} \quad (1)$$

where A is the signal amplitude. This definition of S corresponds to the S_{14} index of Briggs and Parkin².

The angle-of-arrival fluctuations were measured by the rms traverse angle σ_{TR} and the rms elevation angle σ_{EL} . In each case the rms values were calculated after removing a linear trend by fitting a straight line to the 45 sample points. The trend correction allowed for relatively slow changes, which were present in addition to the more rapid fluctuations produced by ionospheric scintillations.

Figure 2 is an example of the plots produced by the post-processing program, which calculates three-second values of track parameters. The geographic and invariant latitude scales are subionospheric latitudes assuming an ionospheric penetration point at a height of 300 km. Millstone Hill is at an invariant latitude of 56°N.

In the condensed form (three-second averages) all the results for the 2376 satellite tracks were stored on two magnetic tapes, so greatly facilitating a statistical analysis of the scintillation data. Values of the geomagnetic disturbance index K_p and local vertical incidence ionosonde measurements of the F-region critical frequency f_oF2 for each track were included on the condensed data tapes.

A small level of signal amplitude fluctuation was evident during all satellite tracks which is not caused by ionospheric scintillation. This produces a "baseline" level for the measured scintillation parameters, which is evident in Figure 2. The baseline level is elevation angle dependent and is typically 0.05 for S . The two major sources of amplitude fluctuations

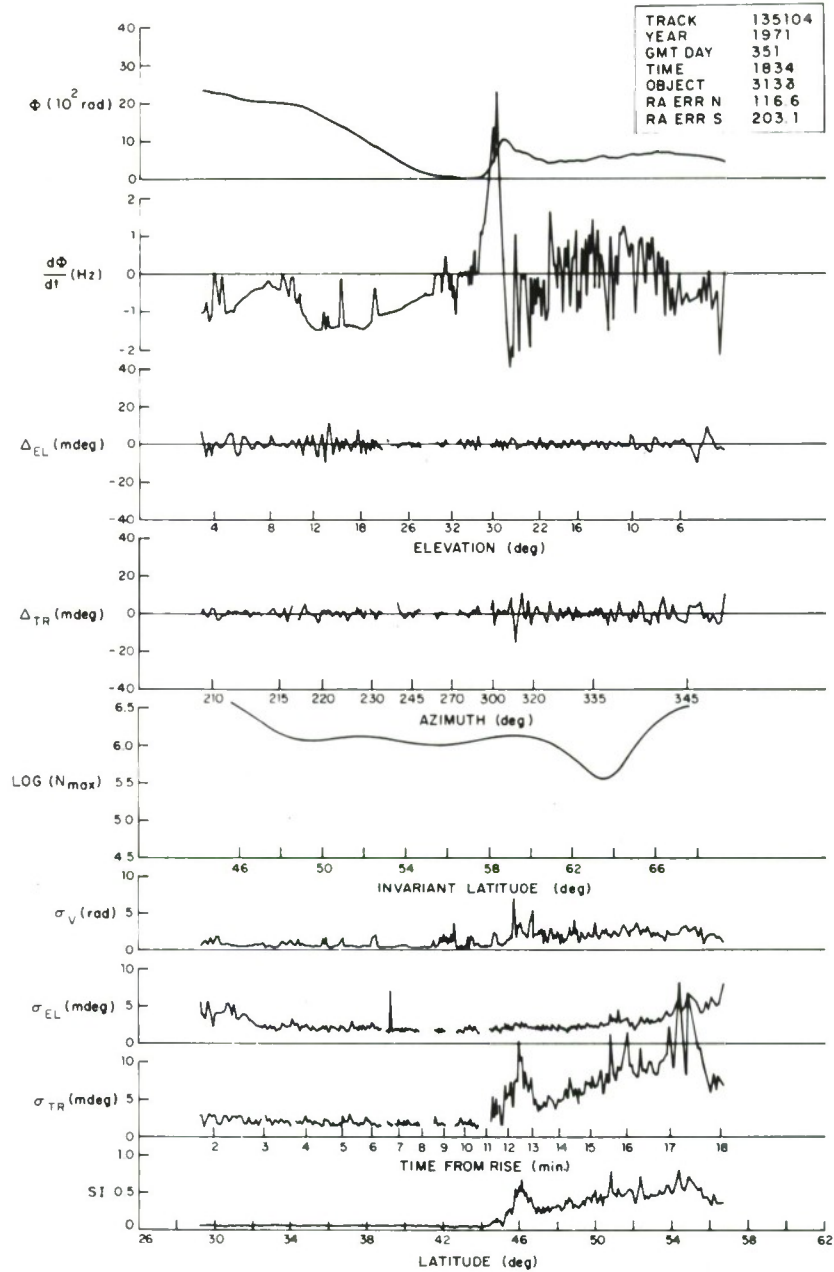


Fig. 2 Typical results for a satellite track obtained for the Millstone Hill propagation study. Starting from the top are (a) UHF-VHF differential phase Φ , (b) differential-doppler $d\Phi/dt$, (c) UHF elevation deviations (3-sec vs 63-sec running means), (d) UHF traverse deviations (3-sec vs 63-sec running means), (e) Log_{10} of peak electron density (f) differential-phase standard deviation, (g) UHF elevation standard deviation, (h) UHF traverse standard deviation, and (i) UHF scintillation index.

causing the baseline level were receiver noise and modulation on the satellite beacon signals, although tropospheric scintillation may also have been present at low elevation angles on some occasions. A model of the baseline variation was constructed and subtracted from the measured scintillation levels to give the scintillation index produced by ionospheric irregularities alone.

C. Differential-Doppler Experiment

The UHF and VHF beacon signals were combined to determine the differential-doppler $d\Phi/dt$,

$$\frac{d\Phi}{dt} = \frac{d}{dt} \left[\text{VHF phase angle} - 3/8 \text{ UHF phase angle} \right] \quad (2)$$

Employing the differential-doppler effectively eliminates doppler changes produced by the changing path length as the satellite moves, thereby, leaving only the changes produced by the ionosphere.

The differential-doppler $d\Phi/dt$ was essentially proportional to the rate of change of electron content along the propagation path from the satellite to antenna. A method of integrating this measurement to determine the variation of the differential phase Φ and the peak electron density N_m along the satellite track is described in detail by Evans and Holt³. Electron density profiles of the Chapman type were assumed at all latitudes and normalization was achieved using the local determination of N_m from ionosonde measurements. Figure 2 includes a plot of $\log_{10} N_m$ derived in this manner.

The differential-doppler records were used directly to give information on the occurrence of long-wavelength traveling ionospheric disturbances which can produce refraction and range errors. The derived parameter N_m permitted a study of the location of the mid-latitude electron density trough which also can produce anomalous propagation effects. The differential phase Φ was especially useful in this propagation study as it is proportional to the ionospheric range error.

D. Refraction Measurements

The L-band radar tracked the Navy Navigation satellites and provided a position estimate which was independent of that provided by the 400 MHz beacon tracker. Ionospheric refraction at L-band is negligible in comparison to that at 400 MHz and the two sets of measurements could be used to directly determine the gross ionospheric refraction at 400 MHz.

To this end, tracking exercises were conducted over intervals of four-five days to gather sufficient L-band data to solve for the orbit of each satellite as well as certain instrumental radar biases. The true satellite positions established in this manner were then compared with the positions given by the beacon tracker. A nighttime comparison (when ionospheric refraction is negligible) allowed further instrumental effects present in the beacon tracker to be evaluated. Finally, the daytime passes were analyzed to determine the refraction produced by the ionosphere at 400 MHz.

A separate investigation of UHF refraction errors was undertaken by comparing the 3-second average elevation (and traverse) angle with the 63-second mean (Figure 2). The procedure eliminated the need for orbit determinations and was suitable for investigations of the refraction errors produced by short-wavelength traveling ionospheric disturbances.

III. ELEVATION ERRORS PRODUCED BY THE AMBIENT IONOSPHERE

A radiowave propagating through the ionosphere and troposphere undergoes bending because of the change in refractive index (n) along the path. In the ambient ionosphere vertical gradients in refractive index are normally much larger than any horizontal ones. Consequently, the primary ionospheric effects may be estimated by assuming spherical symmetry which results in (n) being a function of altitude only. Some departures from the case of spherical symmetry are discussed in later sections.

With the refractive index a function of altitude only, Snell's law takes the form

$$n r \cos E = n_0 r_0 \cos E_0 \quad (3)$$

and the total bending $\Delta\alpha$ (Figure 3) is expressed as

$$\Delta\alpha = - \int_0^{h_T} \frac{n_0 r_0 \cos E_0 \frac{dn}{dh} dh}{n \left[n^2 (r_0 + h)^2 - n_0^2 r_0^2 \cos^2 E_0 \right]^{\frac{1}{2}}} \quad (4)$$

where E_0 and n_0 are the apparent elevation angle and refractive index at the earth's surface, h_T is the height of the target and r_0 is the earth's radius.

The total bending is expressed as the sum of the ionospheric and tropospheric components,

$$\Delta\alpha = \Delta\alpha_I + \Delta\alpha_T \quad (5)$$

In the troposphere $n > 1$ and dn/dh is negative causing $\Delta\alpha_T$ to be positive and the apparent elevation to exceed the true elevation. The refractive index of the ionosphere for radiowave frequencies (f) in the VHF range or higher is approximately given by

$$\begin{aligned} n &= \left[1 - \frac{e^2 N}{4\pi^2 \epsilon_0 m f^2} \right]^{\frac{1}{2}} \\ &= \left[1 - \frac{f_p^2}{f^2} \right]^{\frac{1}{2}} \end{aligned} \quad (6)$$

where N is the electron concentration, ϵ_0 the permittivity of free space, e the electron charge, m the electron mass and f_p the plasma frequency. The electron density N is always small below 60 km, reaches a maximum at height h_m (around 250-350 km) and decreases above h_m (Figure 1). For a radar target above a plane ionosphere there would be no ionosphere bending since the ray path is from a region where $n = 1$ above the ionosphere, to a region between the ionosphere and troposphere where n is again unity. However, for a

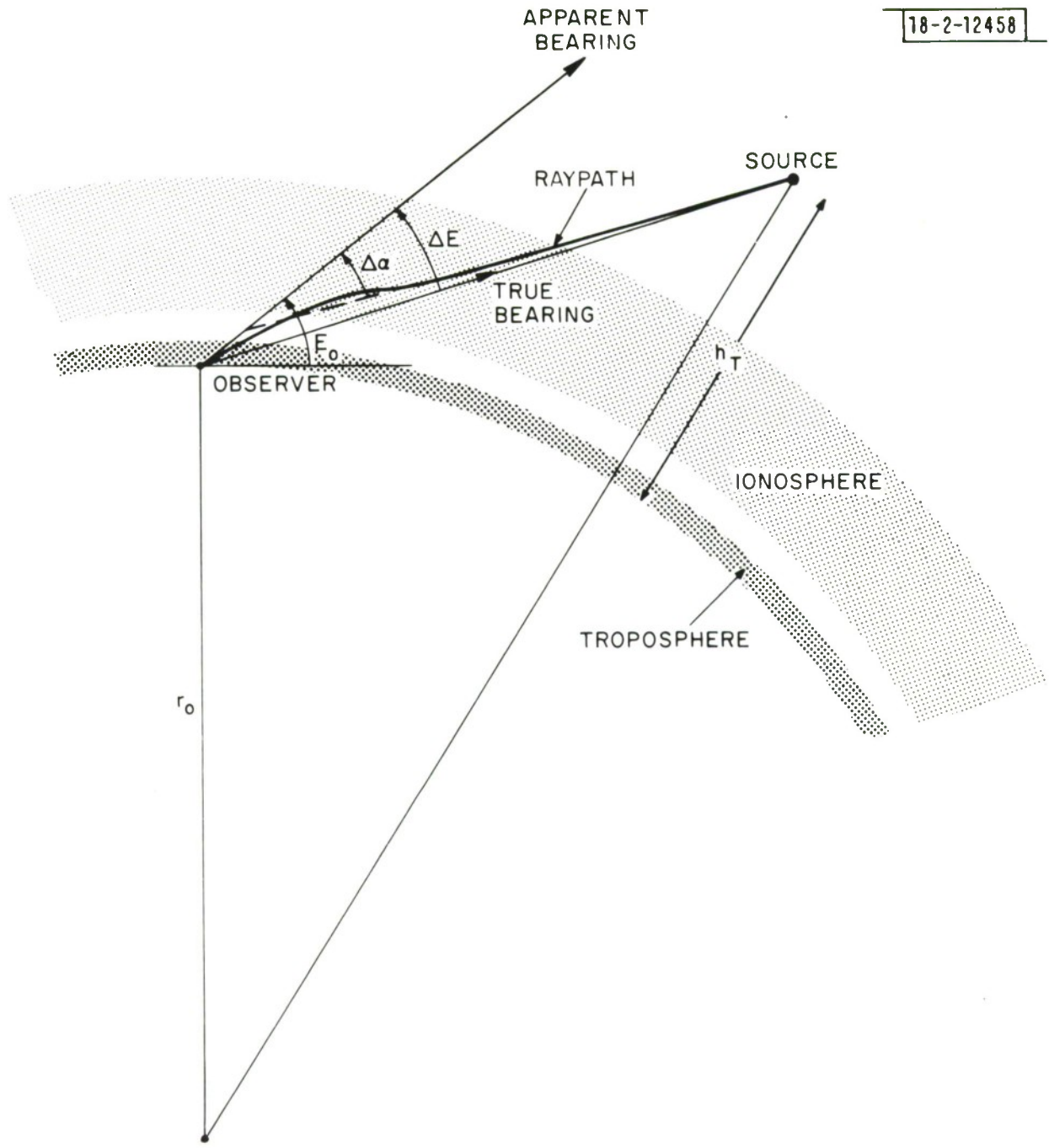


Fig. 3 Complete ray-path through the troposphere and ionosphere.

curved ionosphere the upward bending above h_m (where dn/dh is positive) is more than compensated by the downward bending below h_m (where dn/dh is negative). Thus, the refraction produced by both the ionosphere and troposphere is in the same sense and increases the apparent elevation angle over the true elevation angle.

In contrast to tropospheric refraction, there is not a rapid increase in ionospheric refraction with decreasing elevation angle. This arises because the height of the ionosphere is non-negligible in comparison with the earth's radius, and there is no way for a ray from the earth to arrive at the ionosphere at grazing incidence. As a result, ionospheric refraction increases slowly as the apparent elevation angle approaches zero and becomes relatively constant over the last few degrees.

The total bending $\Delta\alpha$ and the elevation error ΔE (Figure 3) may be calculated once the refractive index is specified as a function of height. However, it is not generally possible to derive analytical expressions for a realistic ionosphere, and a ray tracing approach must be used to determine $\Delta\alpha$ and ΔE . Accurate calculations of ionospheric refraction must include the tropospheric component of refraction, as this alters the angle of incidence of the ray at the ionosphere. The ionospheric component of elevation angle error ΔE_I may be obtained from

$$\Delta E_I = \Delta E_{TOT} - \Delta E_T \quad (7)$$

where ΔE_{TOT} results from the combined ionosphere and troposphere and ΔE_T is the result for the troposphere alone.

The ionospheric component of elevation error ΔE_I has been investigated at BTL⁴ using ray tracing techniques and electron density profiles of the Chapman form

$$N(h) = N_m \exp \frac{1}{2} (1 - z - e^{-z}) \quad (8)$$

with

$$z = \frac{h - h_m}{h_s}$$

and h_s is the scale height of the ionizable neutral gas and N_m is the peak electron density at height h_m . The plasma frequency at the peak f_m (i.e., the critical frequency f_oF2) is related to N_m by

$$f_m = 8.98 N_m^{\frac{1}{2}} \quad (9)$$

where f_m is in the Hz and N_m in electrons/m³. We have found that the BTL ray tracing results for ΔE_I can be fitted reasonably well by an empirical formula of the form

$$\Delta E_I = 31.2 \times 10^3 \left(\frac{f_m}{f} \right)^2 \frac{\cos E_o \exp \left[- E_o^2 / (21.4 + 57.0 \exp (-h_T/393)) \right]^2}{1 + \exp \left[(h_m - h_T) / .75 h_s \right]} \text{mdeg} \quad (10)$$

where the apparent elevation angle E_o is in degrees and the target height h_T is in km. Equation 10 is applicable for typical ionospheric values of h_m (250-350 km) and h_s (40-60 km).

Some of the BTL ray tracing results for Chapman profiles are shown in Figures 4 and 5 as functions of target height and apparent elevation angle. Also shown in the figures is the empirical fit given by equation 10. The range of elevation angles available from the ray tracing program is quite limited (Figure 5) and the empirical fit could be inadequate for $E_o > 20^\circ$.

Ray tracing studies were also conducted by BTL using actual electron density profiles as measured by the Millstone Hill incoherent scatter radar, rather than profiles having an assumed Chapman form. The calculations used $h_T = 1000$ km and $f = 400$ MHz. Results were scaled to $f = 1000$ MHz using a f^{-2} scaling law, and the diurnal variation of ΔE_I is shown in Figure 6 for observations made on 23-24 Feb. 1970. On these days f_m attained a maximum daytime value of 12 MHz and an elevation error of about 4.5 mdeg would be expected at low elevation angles for $f = 1000$ MHz. The predictions from the empirical formula using the measured diurnal variation of f_m are compared with the ray tracing results in Figure 7, for selected elevation angles of 2° , 10° and 30° . The agreement is reasonable for the

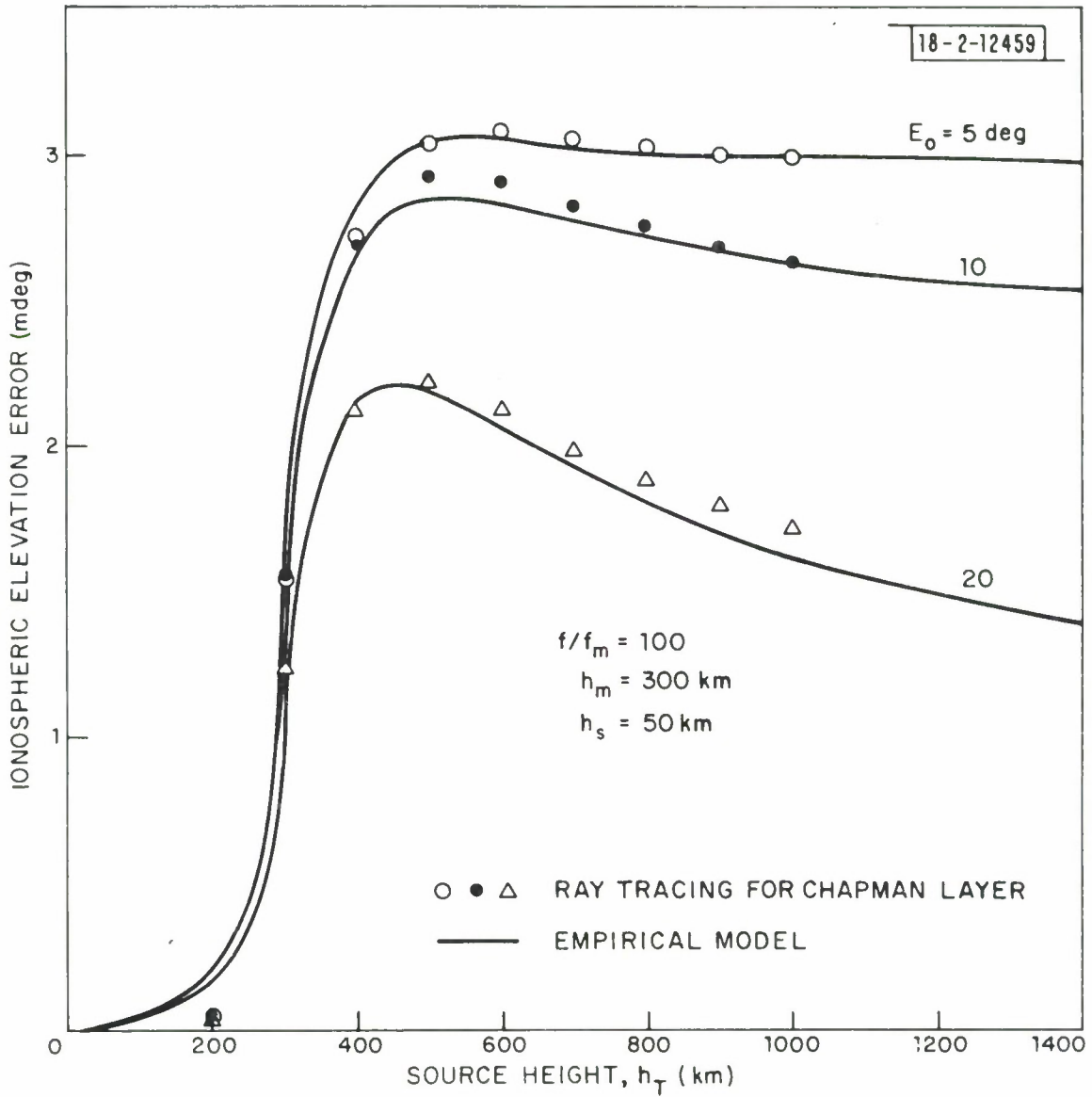


Fig. 4 Ionospheric elevation errors as a function of target height obtained from ray-tracing through Chapman layers are compared with the empirical model given in the text.

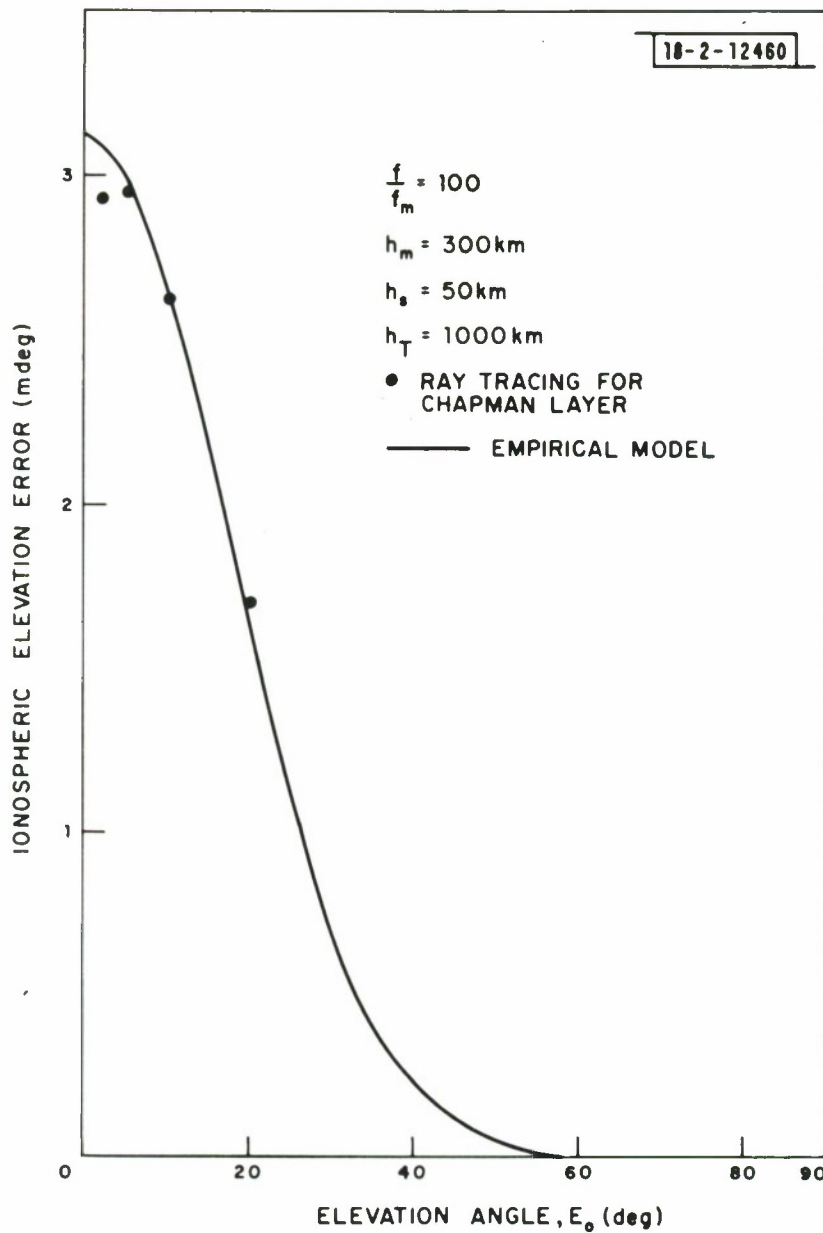


Fig. 5 Ionospheric elevation errors as a function of apparent elevation obtained from ray-tracing through Chapman layers are compared with the empirical model.

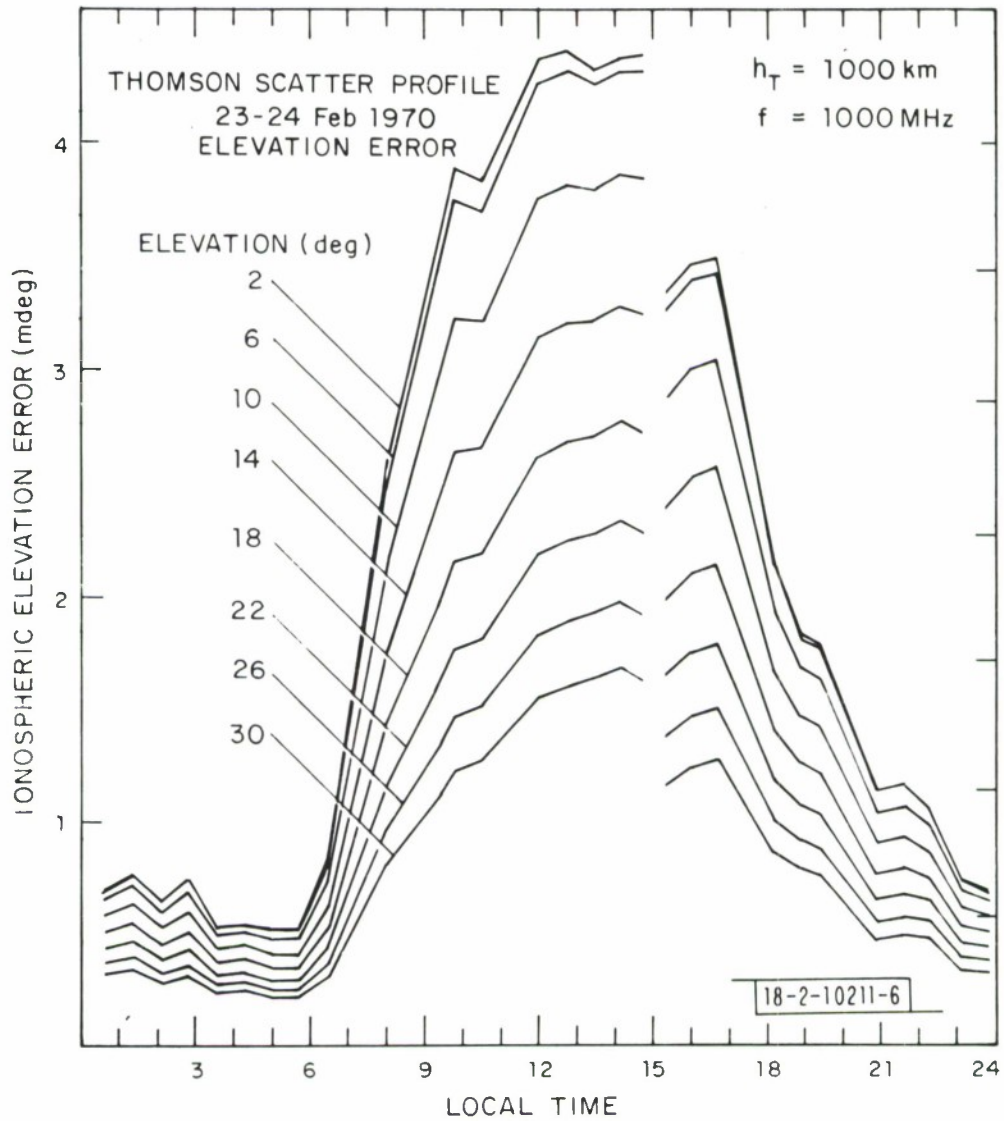


Fig. 6 Ionospheric elevation error at 1000 MHz computer by ray-tracing through profiles such as those shown in Figure 1 for a 24-hour period in February 1970.

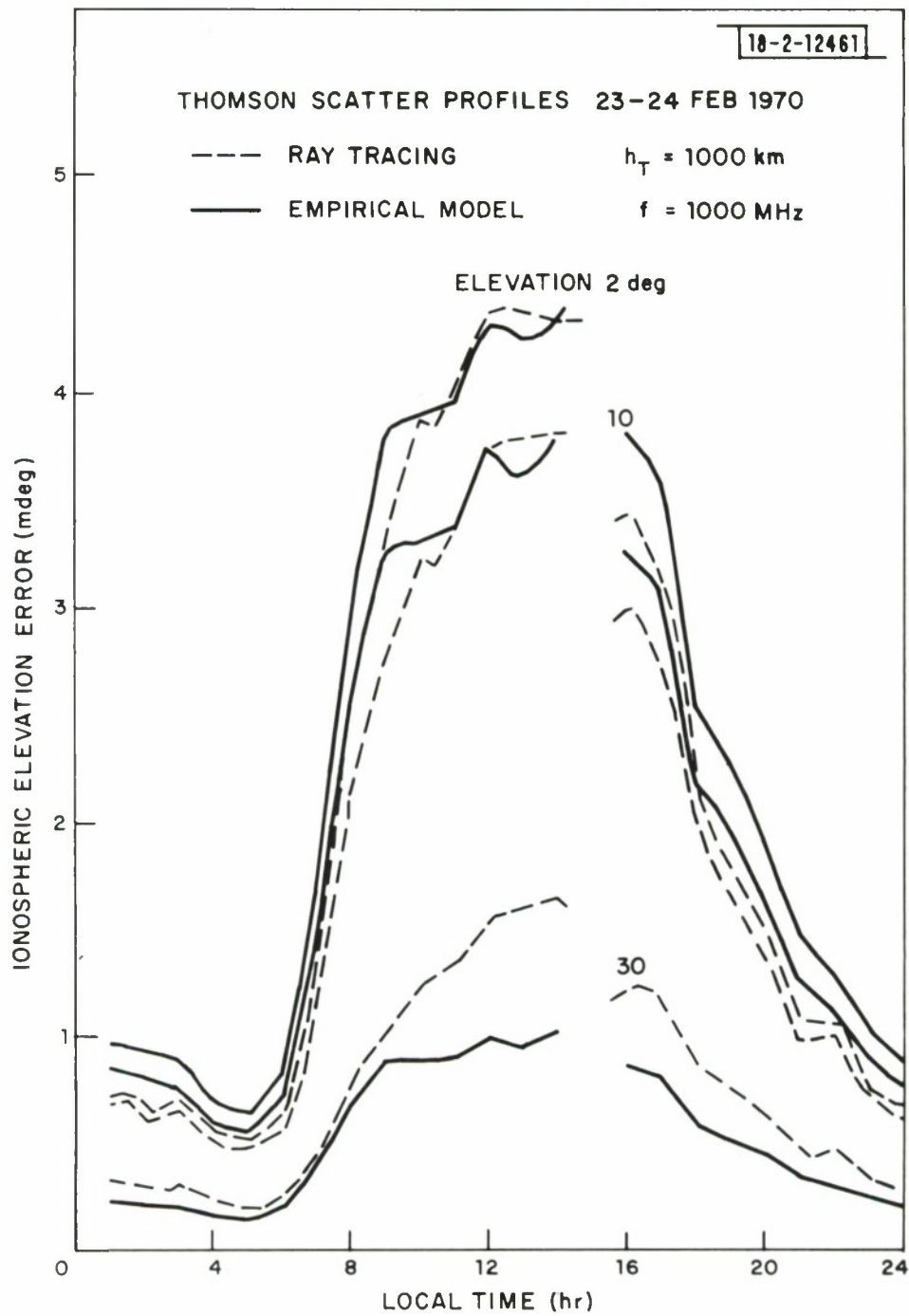


Fig. 7 Comparison of elevation errors given in Figure 6 with the predictions from the empirical model.

smaller values of E_o , but not so good for $E_o = 30^\circ$ under daytime conditions.

A further test of the empirical model (equation 10) was made by comparing it with elevation error measurements made at Millstone Hill (Section II). The observing frequency was 400 MHz, and the Millstone Hill results in Figure 8 represent the average for seven satellite tracking periods between August 72 and March 73¹. The satellite height was 1000 km and the mean value of f_m was 7.8 MHz (daytime conditions). The predictions from the empirical model provided an excellent match to the measurements (Figure 8).

Based on equation 10 the elevation error produced by the ionosphere can be estimated for any operating frequency, elevation angle and target height, once the ionospheric parameters h_m , h_s and f_m are known. Elevation errors are largest in daytime when typical values of h_m and h_s are 300 km and 50 km, respectively. The most important parameter in determining the elevation error is f_m , which undergoes large diurnal, seasonal and sunspot cycle variations. The maximum values of f_m at mid and high latitudes occur during winter daytime at sunspot maximum, and only rarely will f_m exceed 15 MHz under these conditions. Thus, for an operating frequency of 1000 MHz and a target height of 1000 km a maximum elevation error of about 7 mdeg could be expected at low elevation angles.

In practice f_m could be obtained from ionosonde measurements made at a point beneath the intersection of the ray-path and the level h_m . Alternatively, predictions of f_m such as those published by the Institute for Telecommunications Services (U.S. Dept. of Commerce, Boulder, Colorado), can be used. This last approach is more convenient but less accurate since the predictions can be in error, especially during magnetically disturbed periods.

IV. RANGE ERRORS IN THE AMBIENT IONOSPHERE

In this section we examine the magnitude of the range errors introduced by the unperturbed (spherically symmetric) ionosphere. The one-way transmission time t for a radar pulse is given by

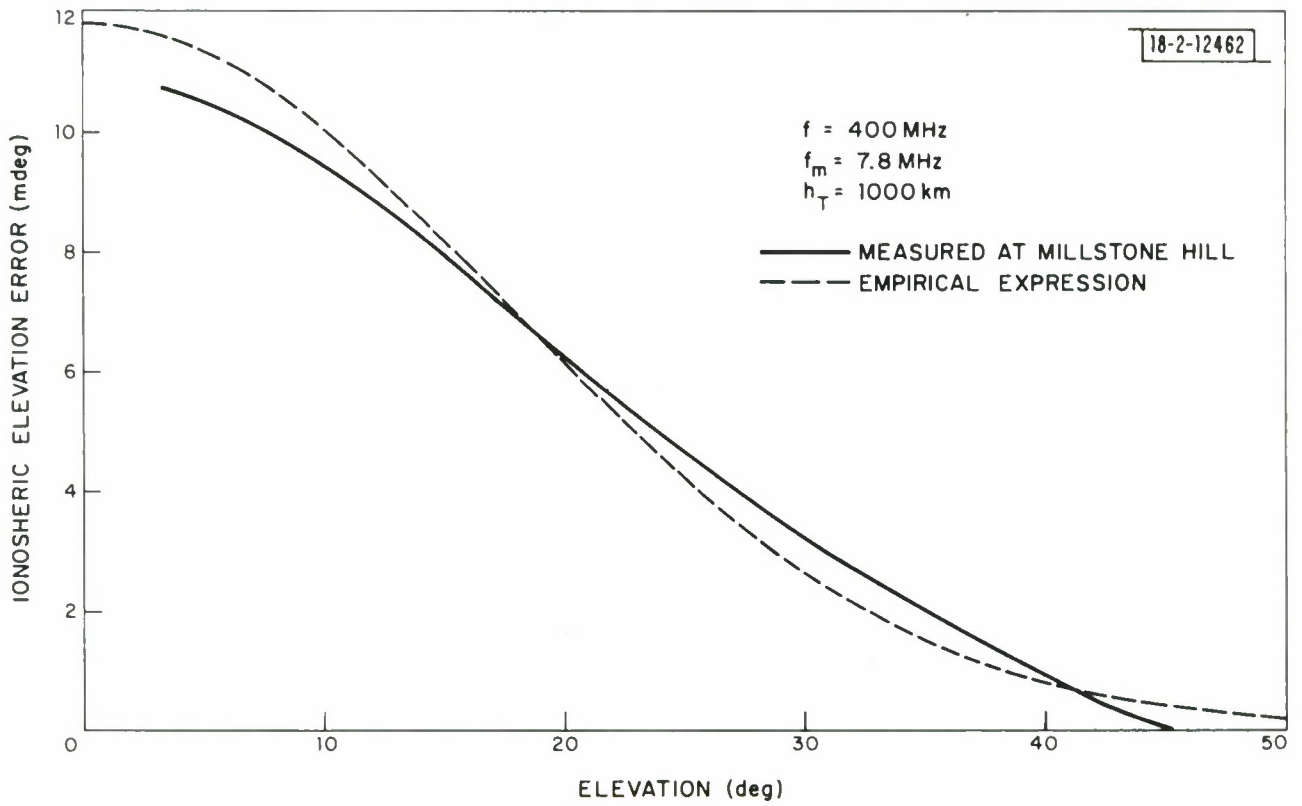


Fig. 8 Comparison of elevation errors measured during the Millstone Hill propagation study at 400 MHz, and predictions from the empirical model.

$$t = \frac{1}{c} \int_0^R n' dr \quad (11)$$

where n' is the group refractive index, and the integral is evaluated along the ray-path from the radar to the target. As n' is greater than unity in the ionosphere, t will exceed the free-space propagation time and cause an increase in the apparent range $R_A = ct$ over the line-of-sight range R . The ionospheric radar range error is expressed as

$$\begin{aligned} \Delta R &= R_A - R \\ &= \int_0^R n' dr - R \end{aligned} \quad (12)$$

The group refractive index may be calculated from

$$n' = n + f \frac{dn}{df} \quad (13)$$

where the ionospheric refractive index n for frequencies f above VHF is given by equation 6. It follows that for the ionosphere $nn' = 1$.

Neglecting ray curvature in the ionosphere and troposphere

$$\begin{aligned} \Delta R &= \int_0^R n' dr - R \\ &\approx \frac{e^2}{8\pi^2 \epsilon_0 m f^2} \int_0^R N dr \end{aligned} \quad (14)$$

Thus, for high radar frequencies f , the ionospheric range error is inversely proportional to f^2 and directly proportional to the electron content along the line-of-sight to the target.

The Chapman electron density profile (equation 8) may be directly integrated for vertical incidence to give a total electron content proportional to $f_m^2 h_s$, where f_m is given by equation 9. In a spherically symmetric ionosphere the total electron content at other elevation angles may be approximated by multiplying the vertical incidence expression by $\sec \chi$, where χ is the zenith angle at the point where the line-of-sight intersects the F2 layer maximum at height h_m . Thus, for a Chapman layer we have the approximate relationship,

$$\int_0^{\infty} N dr \propto f_m^2 h_s \sec \chi \quad (15)$$

The angle χ is given by

$$\sin \chi = \frac{r_o \cos E_o}{r_o + h_m} \quad (16)$$

where r_o is the earth's radius.

Ray-tracing methods were used at BTL⁴ to determine ionospheric range errors for various target heights and elevation angles using electron density profiles of the Chapman form (equation 8). As the BTL calculations were only available for elevation angles $\leq 20^\circ$, they were supplemented with results from GE⁵, which covered the full range of elevation angles. (The GE model included additional ionization at E and F1 region heights and gave slightly different results than the BTL model.)

A fit was made to the two combined sets of ray-tracing results to provide an empirical expression of the form

$$\Delta R = \left(\frac{f_m}{f} \right)^2 \frac{1.97 h_s \sec \chi}{1 + \exp \left(\frac{1.15 h_m - h_T}{1.12 h_s} \right)} \text{ meters} \quad (17)$$

where h_s is given in meters. The form of equation 17 is based on the approximate expression for a target at infinity (equations 14, 15) together with an added empirical term in the denominator to allow for the dependence on target height h_T . The empirical fit given by equation 17 is compared with some of the ray-tracing data in Figures 9 and 10.

Ray-tracing results were also performed at BTL⁴ with electron density profiles measured with the Millstone Hill incoherent scatter radar on February 23 and 24, 1970. The calculations assumed spherical symmetry and took $h_T = 1000$ km and $f = 400$ MHz. The results, scaled for $f = 1000$ MHz using an f^{-2} law, are shown in Figure 11 as a function of local time and elevation angle. The maximum value of f_m was 12 MHz for these data and the corresponding maximum range error was 48 m.

Predictions from the empirical formula (equation 17) based on the measured diurnal variation of f_m on February 23 and 24, 1970, are compared with the ray-tracing results in Figure 12 for elevation angles of 2° , 10° and 30° . In general, a satisfactory agreement is attained.

The empirical expression for range error (17) was further checked by comparing with results from the Millstone Hill satellite tracking program (Section II). Although the ionospheric range errors were not directly measured in this study, the line-of-sight electron content could be estimated and used to predict ΔR at $f = 1000$ MHz via equation 14. The content measurements were based on VHF-UHF differential-doppler measurements combined with local values of f_m at Millstone Hill (Section II). Range errors calculated in this manner are shown in Figures 13, 14 and 15, as functions of elevation angle looking to the south (azimuths 90° to 270°) and looking to the north (azimuths 270° to 90°), for the local values of f_m at Millstone Hill in three ranges (2 to 4 MHz, 8 to 10 MHz and 10 to 12 MHz). Each point represents an average over many satellite tracks; the bar is the standard deviation of the range errors in the particular interval, and thus gives a rough indication of the amount of variability in range error expected for a given local value of f_m . The range errors are generally larger to the south of Millstone Hill because of increased electron concentrations to the south on average. The model pre-

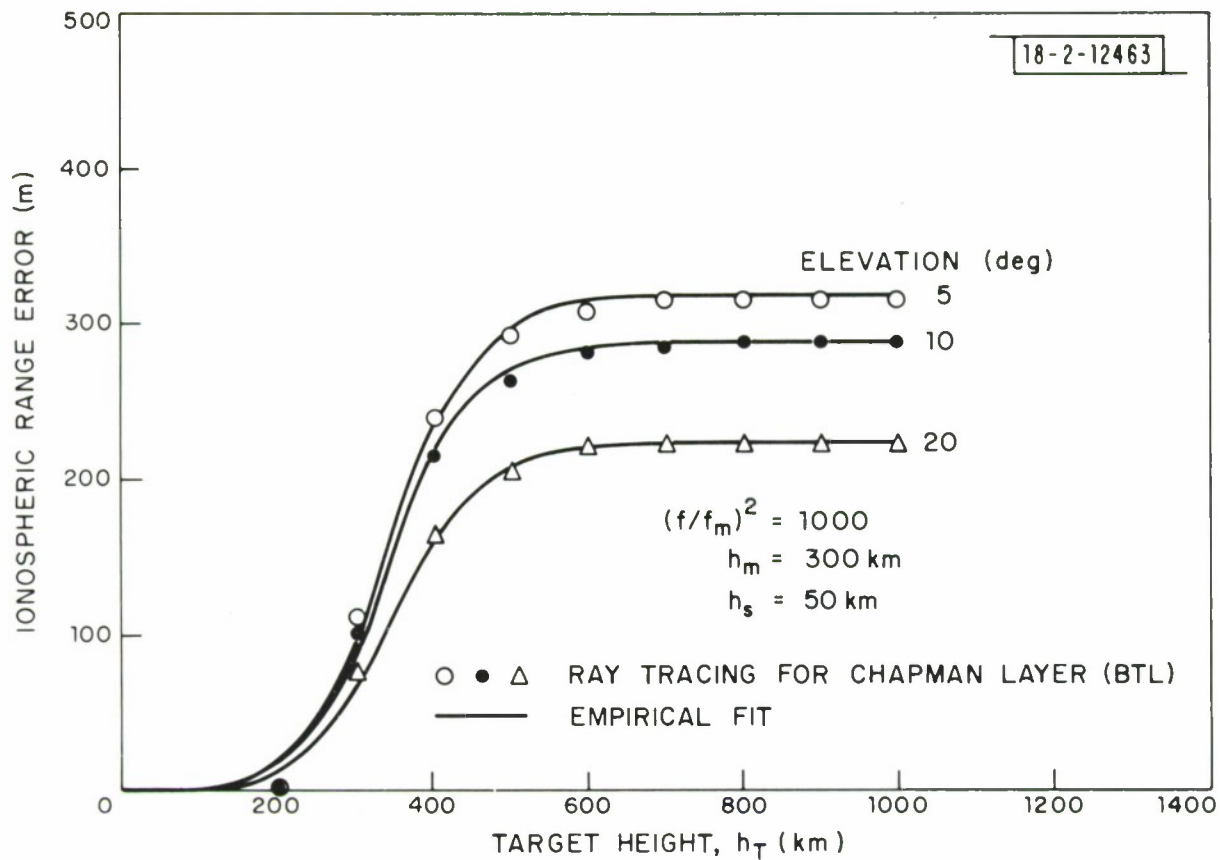


Fig. 9 Ionospheric range errors as a function of target height from ray-tracing through Chapman layers compared with the empirical expression derived in the text.

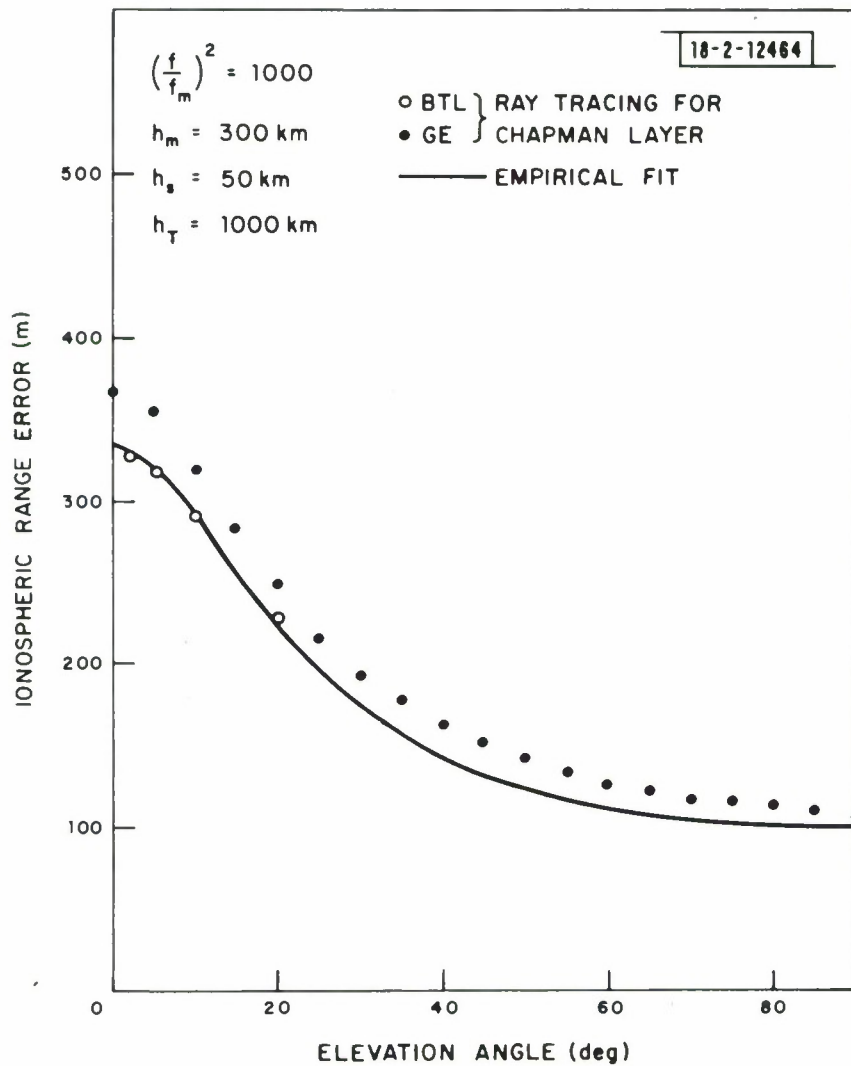


Fig. 10 Ionospheric range errors as a function of apparent elevation angle obtained from ray-tracing through Chapman layers are compared with an empirical model.

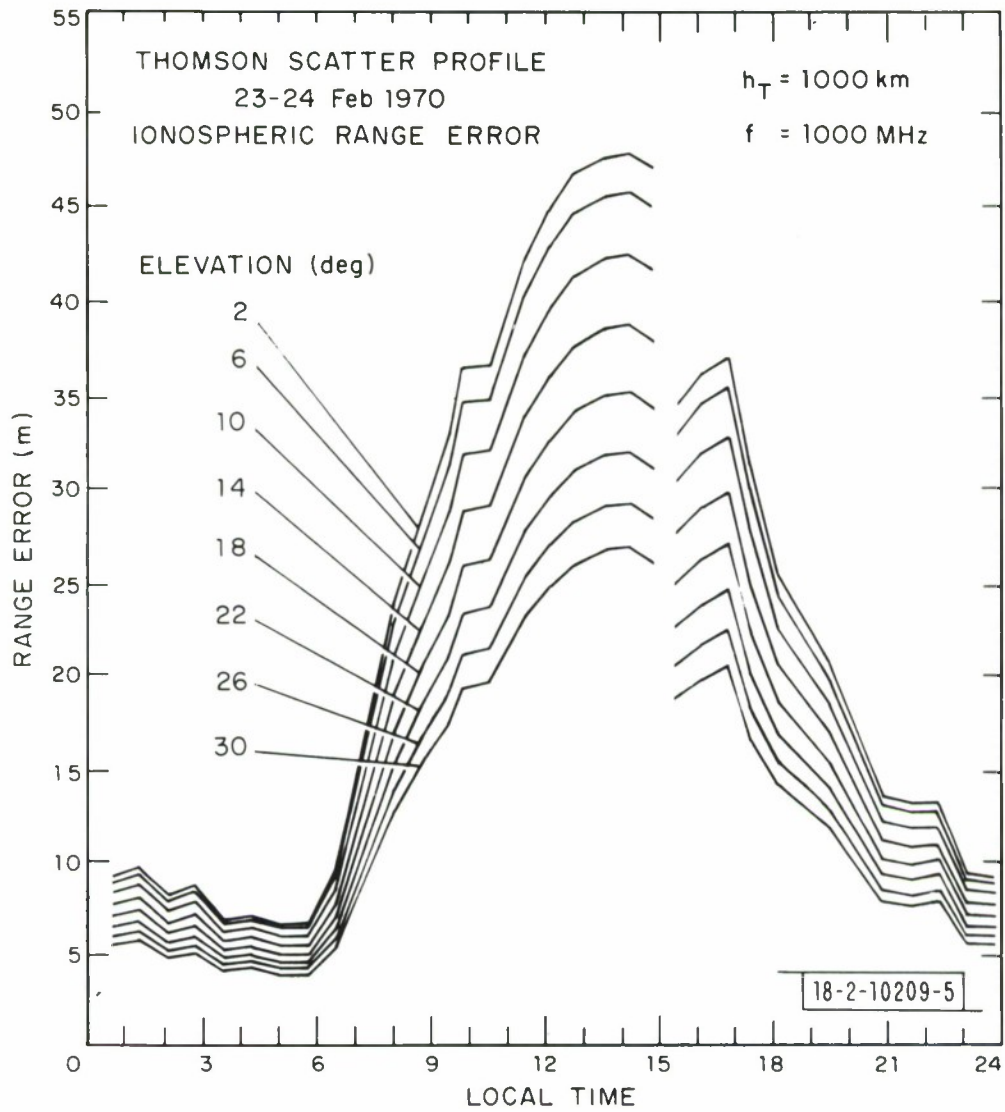


Fig. 11 Ionospheric range error at 1000 MHz computed by ray-tracing through profiles such as that shown in Figure 1 for a 24-hour period in February 1970.

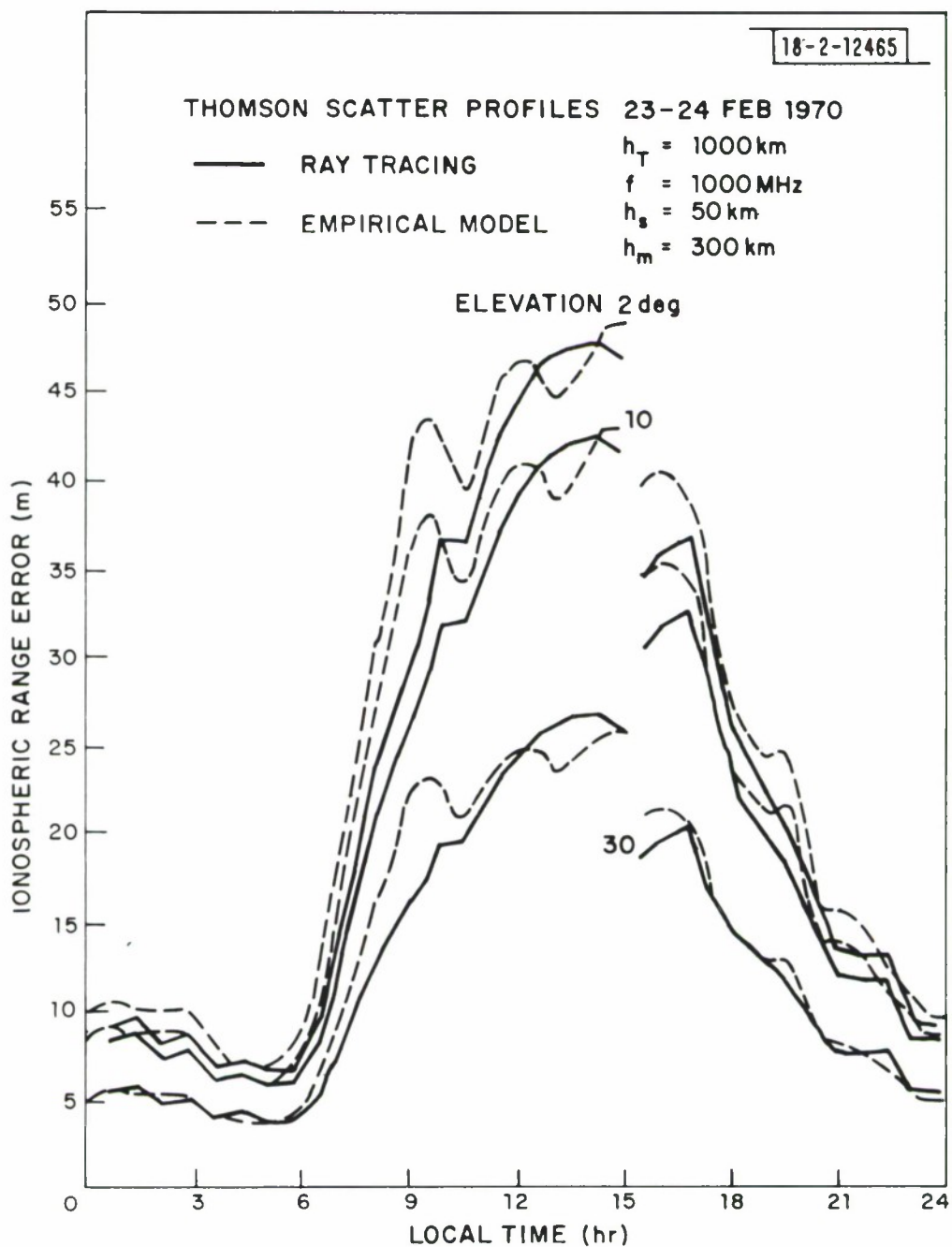


Fig. 12 Comparison of elevation errors given in Figure 11 with predictions from the empirical model.

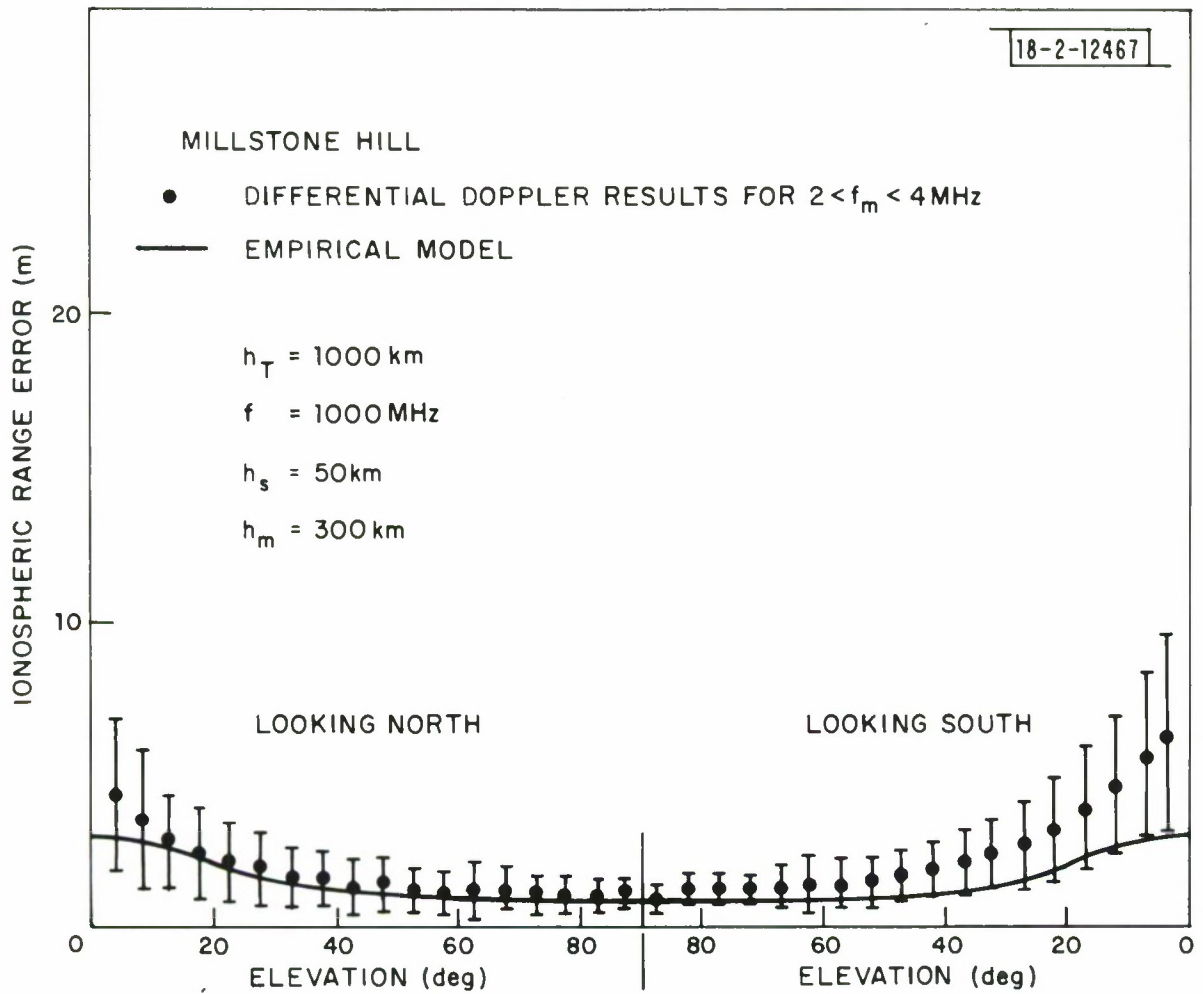


Fig. 13 Comparison of range error predictions from the empirical model and values derived from differential-doppler data recorded during the Millstone Hill propagation study. Results are for a range of local f_oF_2 values (f_m) from 2 to 4 MHz.

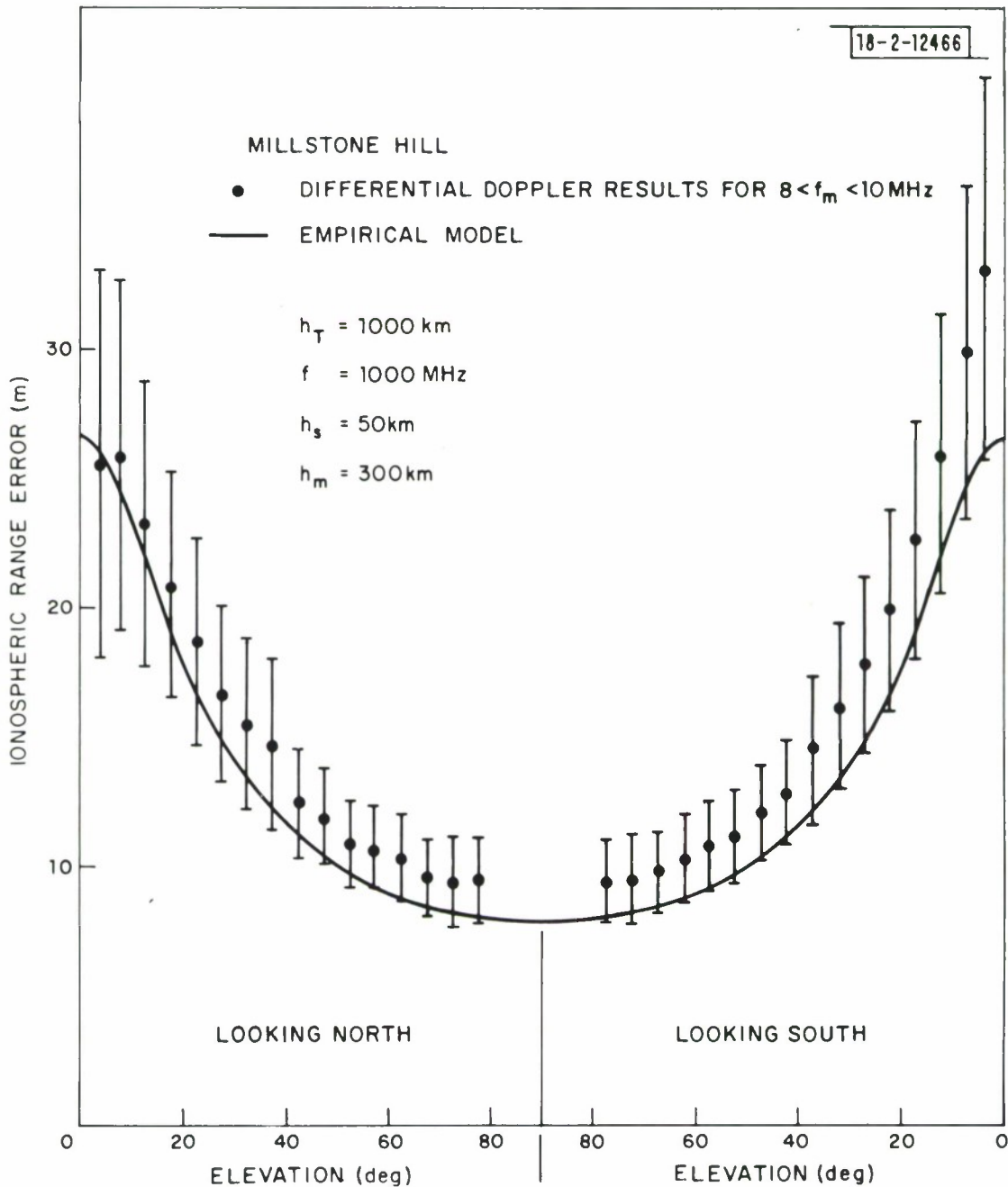


Fig. 14 Comparison of range error predictions from the empirical model and values derived from differential-doppler data recorded during the Millstone Hill propagation study. Results are for a range of local f_oF_2 values (f_m) from 8 to 10 MHz.

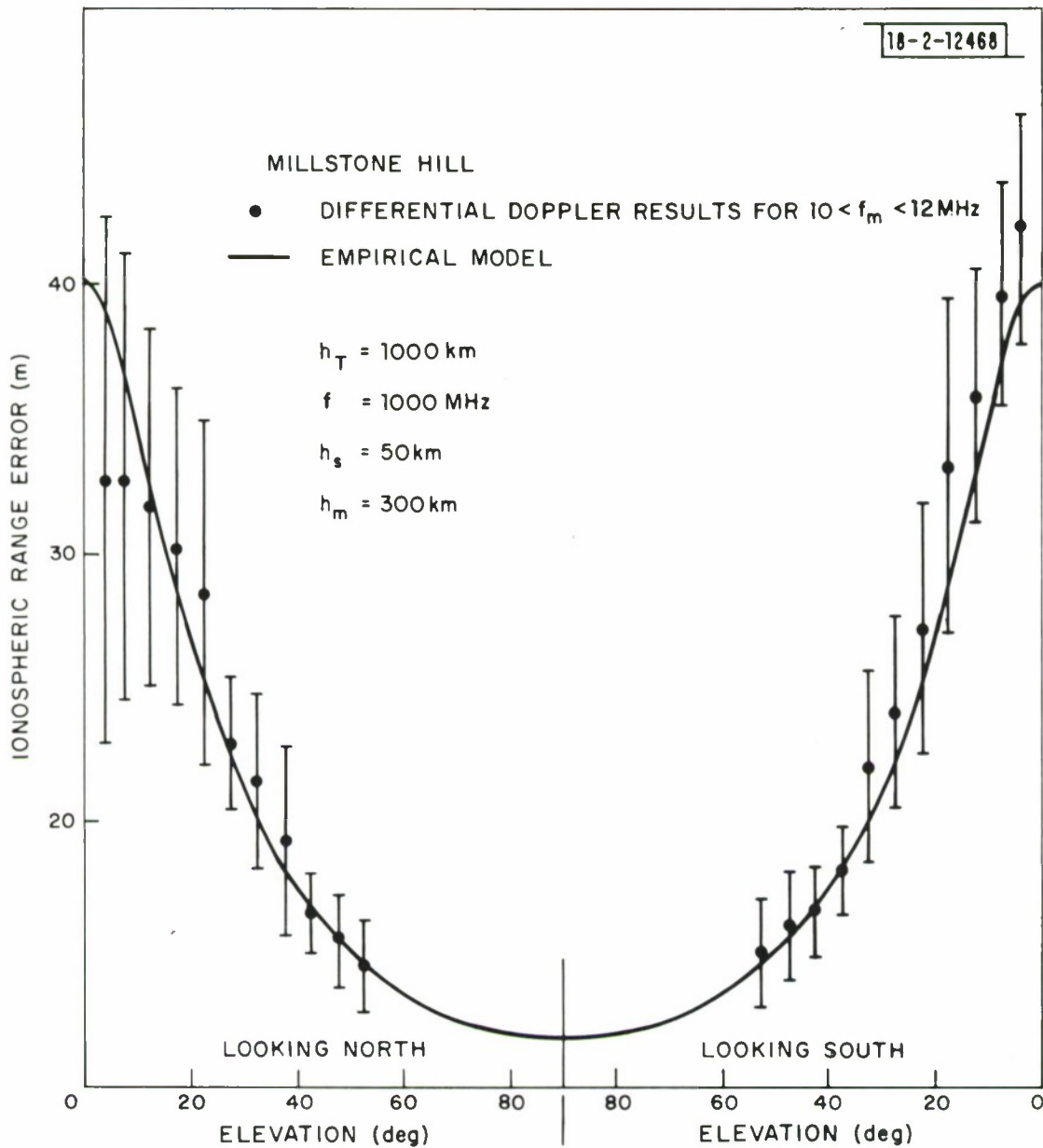


Fig. 15 Comparison of range error predictions from the empirical model and values derived from differential-doppler data recorded during the Millstone Hill propagation study. Results are for a range of local f_oF_2 values (f_m) from 10 to 12 MHz.

dictions are seen to provide a good fit to the data in Figures 13, 14 and 15. As the model is based on spherical symmetry, the north-south variation clearly cannot be matched.

Once the values of the ionospheric parameters f_m , h_s and h_m are supplied, equation (17) provides a prediction of ionospheric range error at any particular operating frequency, target height and elevation angle. Range errors are of most concern during the daytime when f_m reaches a peak. If more precise information is lacking typical daytime values of $h_m = 300$ km and $h_s = 50$ km might be adopted as these parameters are not as important as f_m in determining the range error. The maximum range errors would be encountered at sunspot maximum conditions at high latitudes in winter, where f_m may reach 15 MHz. For an operating frequency of 1000 MHz and a target height of 1000 km the maximum radar range error given by equation 17 is about 75 m at low elevation angles.

From equation 14 it is evident that the ionospheric range error is proportional to the square of the radar frequency. Accordingly, wideband FM systems or other short pulse systems should take this into consideration. For example, a 10% sweep in frequency will produce a -20% change in ΔR . Thus for an FM radar at 1000 MHz, a 10% sweep will produce a range dispersion of about 15 m for the case when the radar range error is ~ 75 m (which is the maximum ever likely to be encountered).

V. HIGH-LATITUDE EFFECTS

A. Auroral Clutter

A number of phenomena occur at high latitudes which can influence radar performance. Auroral radar clutter echoes are observed which are associated with a region known as the auroral oval which encircles the poles between 65° and 80° invariant latitude. These echoes are of concern to a radar looking northward into the auroral zone as they may mask a target approaching the radar when the target is situated at the same range as the clutter. Auroral clutter is most serious when the radar line-of-sight intersects the magnetic field lines in the E-region near perpendicularity. Because of the requirements of this favored geometry the clutter is typically quite limited in range.

An L-band radar study of auroral returns was made at Millstone Hill and is reported in detail by Evans¹. It was found that the mean height of auroral echoes was near 110 km with a mean half-power thickness of < 10 km and that the power fell by 3db when the aspect angle with respect to the magnetic field was increased from 0 to .4°.

B. Electron Density Trough

Anomalous amounts of ionospheric refraction and range error can be introduced at high latitudes by the presence of large horizontal (principally latitudinal) gradients in the electron density. A belt of high density is associated with the auroral oval where visible auroras are most often seen. Equatorwards of the auroral oval, there is a narrow latitudinal belt of low electron density known as the mid-latitude electron density "trough". This feature is evident in the $\log_{10} N_m$ plot in Figure 2 near an invariant latitude of 64°N.

The dependence of the trough location on time and magnetic activity was established using the differential-doppler measurements made in the Millstone Hill satellite tracking study. For each satellite track, the differential-doppler record and local ionograms were used to derive the variation of peak electron density (N_m) with invariant latitude as described in Section II. Mean values of N_m were calculated for two hour intervals of local time and 2° steps of invariant latitude for two six month "seasons" and three K_p intervals. Sample results are given in Figures 16 and 17 as contour plots, with the deduced trough positions also shown. No indication of the daytime position of the trough is evident because it is then usually difficult to identify such a feature. Mean trough positions for the three K_p intervals are given in Figure 18. Averages of the summer and winter positions are shown in Figure 18 as there was little seasonal variation evident for a given K_p level. In general, the trough is seen to move about 2° southward for unit increase in K_p . A similar dependence is given by Rycroft and Thomas⁶.

The trough occurs principally at night when the ambient electron density is low and hence will not usually affect propagation errors in a significant way. However, during magnetically disturbed conditions the trough may be evident during the daytime and cause important propagation anomalies.

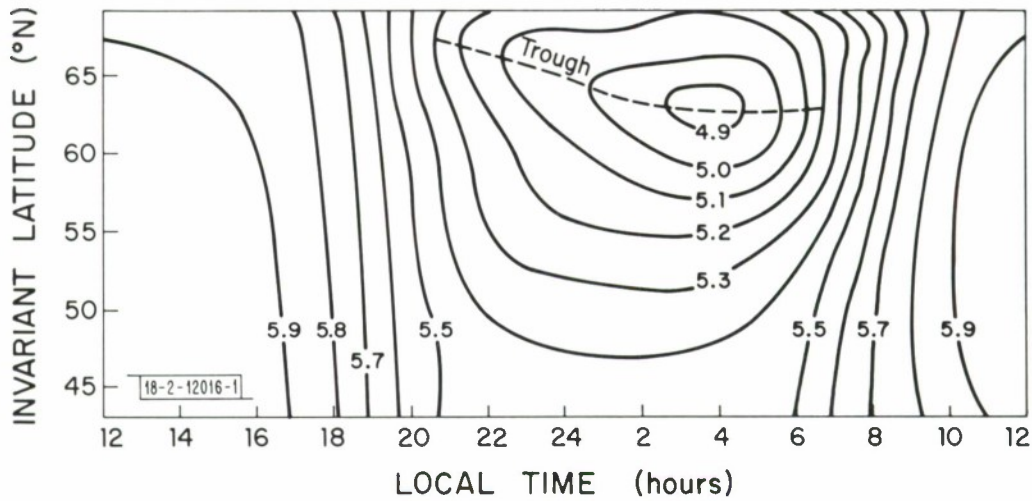


Fig. 16 Contours $\log_{10} N_m$, as derived from differential-doppler measurements made at Millstone Hill 1971-1973. Results are for a K_p interval 0_0 to 1_+ in winter and the deduced mean position of the electron density trough is shown.

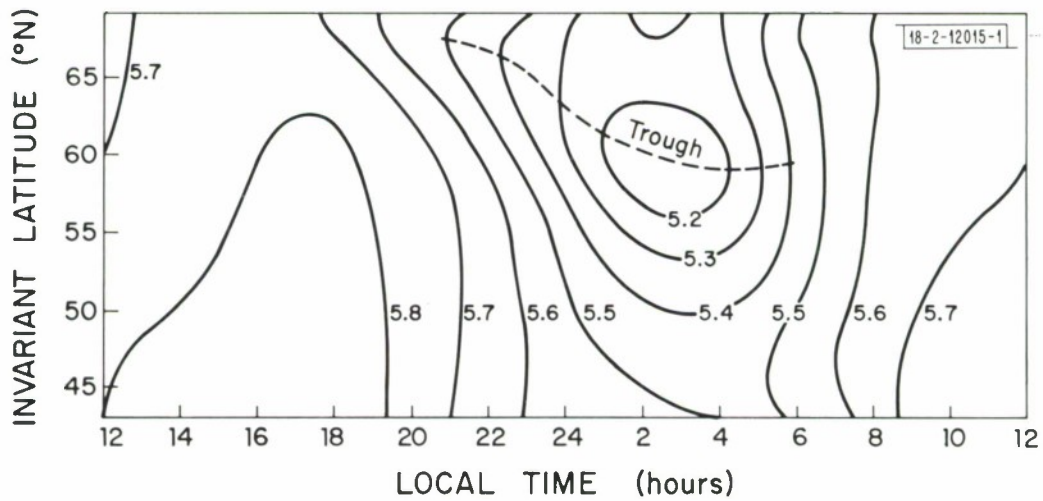


Fig. 17 Contours $\log_{10} N_m$, as derived from differential-doppler measurements made at Millstone Hill 1971-1973. Results are for a K_p interval 2_- to 3_+ in summer and the deduced mean position of the electron density trough is shown.

- Kp 0₀ to 1₊
- - - Kp 2₋ to 3₊
- · - · - Kp 4₋ to 5₊

18-2-12006-1

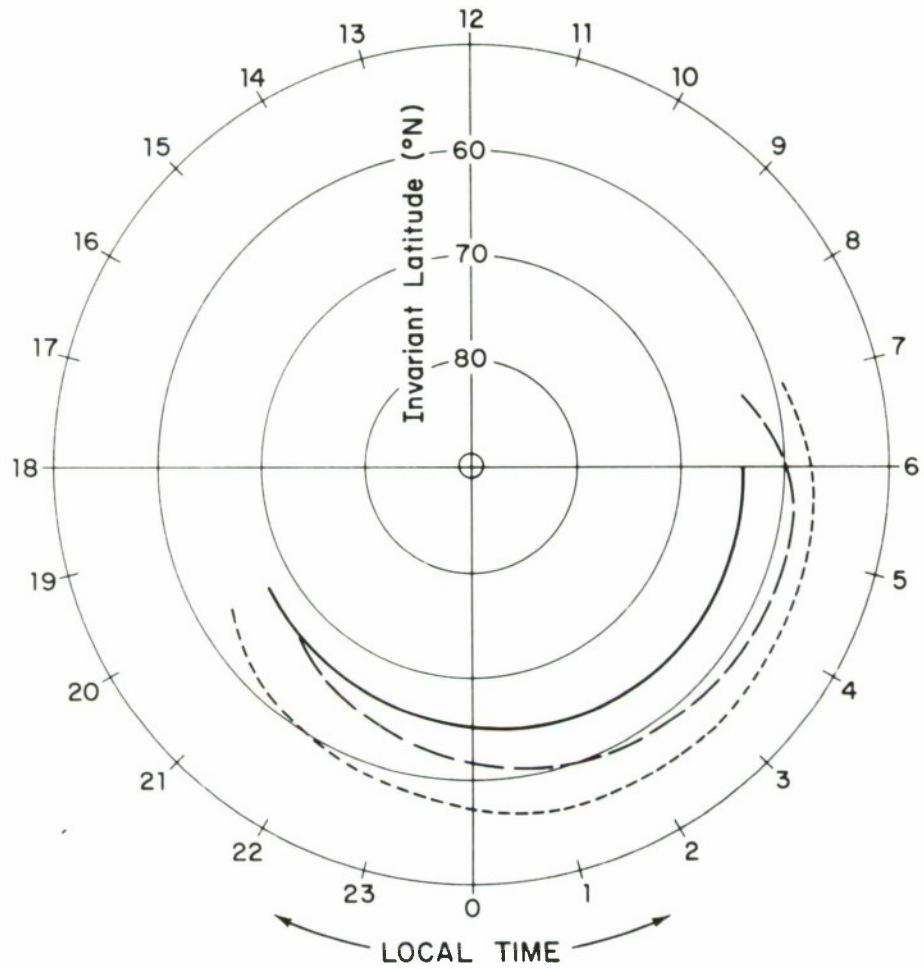


Fig. 18 Mean location of the mid-latitude electron density trough from Millstone Hill differential-doppler measurements.

In the Millstone Hill propagation study the trough was often recognizable on single satellite tracks because of the perturbation introduced in the differential-doppler records. Figure 19a is an example of differential-doppler data gathered on successive daytime passes on one day when the trough could be seen approaching the radar. The UHF elevation residuals for these passes exhibited corresponding perturbations, as shown in Figure 19b. To estimate the trough-induced elevation errors for an L-band radar an f^{-2} scaling law was applied to the measured UHF elevation errors. Thus, Figure 19b includes a scale appropriate to an operating frequency of 1000 MHz and it is seen that in this instance the trough associated refraction errors were about +3 mdeg with a decay after sunset. Ray-tracing studies have established that these positive elevation excursions are associated with rays that traverse the lower ionosphere equatorwards of the trough and emerge above the layer peak in the trough, i.e., where the densities are low. A corresponding negative excursion associated with the polar edge of the trough is not seen, apparently, because the horizontal gradients in density are smaller at the poleward edge and because the required geometry is less readily achieved.¹ Based on the results of the Millstone tracking study at UHF the largest trough-induced elevation errors at L-band would have been about +9 mdeg.

Range errors could also be estimated from the differential-doppler data because both the radar range error and the differential-phase angle introduced by the ionosphere are proportional to the total electron content along the radar line-of-sight to the satellite. For a radar frequency f (in MHz) the ionospheric radar range error (in meters) is given by,

$$\Delta R = \frac{8340 \Phi}{f^2} \quad \text{m} \quad (18)$$

where Φ is the UHF-VHF differential-phase angle in radians. To use this relationship to estimate range errors, it was first necessary to integrate the values of $d\Phi/dt$ obtained along a satellite track and evaluate the constant of integration. The procedure which was implemented assumed electron density profiles of the Chapman type, and used local f_oF_2 measurements to determine the peak electron density (Section II). Figure 19c gives the range errors

18-2-11225-2

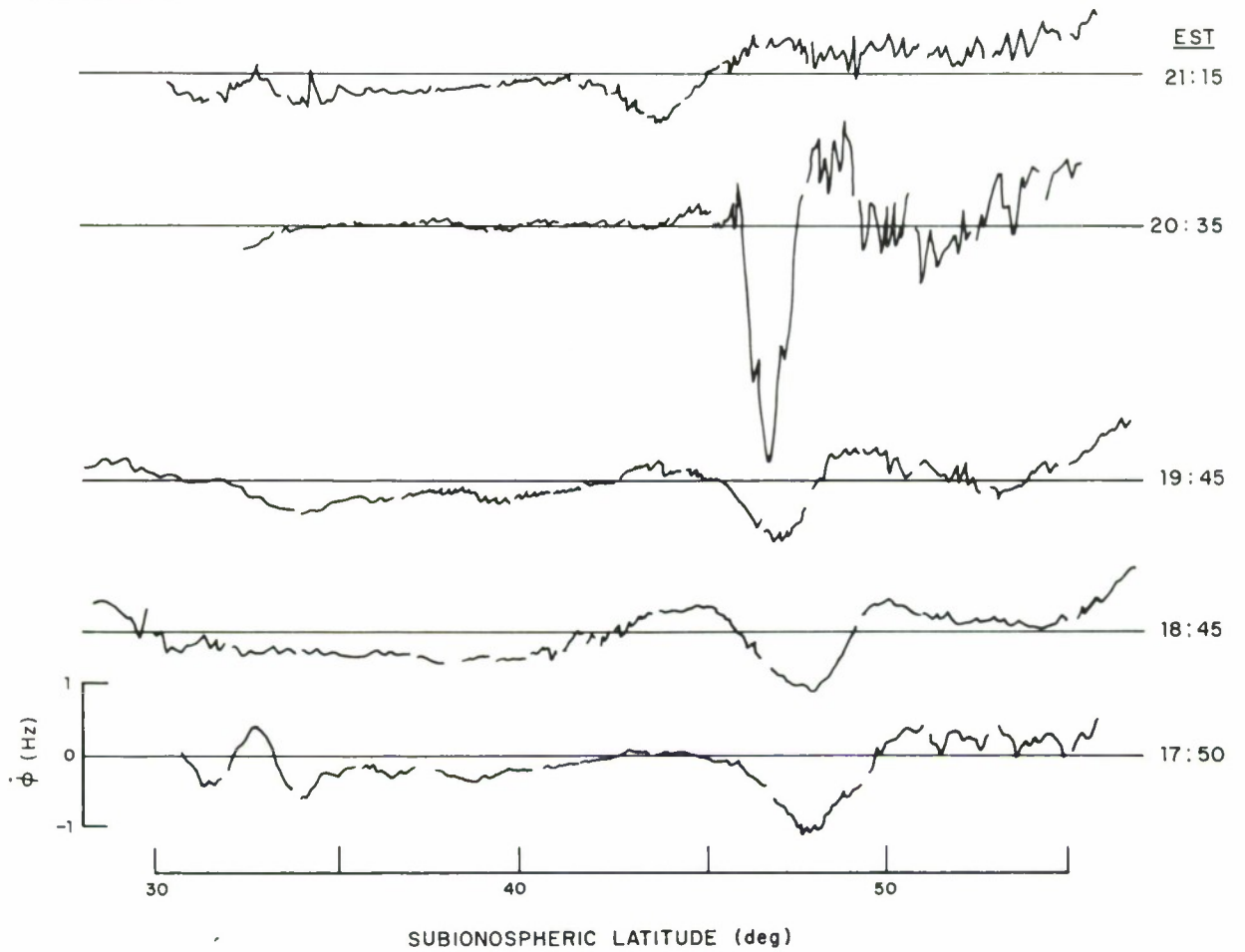


Fig. 19a Successive records on 28 November 1972, (passes of the Navy Navigation Satellites) exhibiting tracking perturbations in UHF-VHF differential-doppler introduced by the presence of the high-latitude trough.

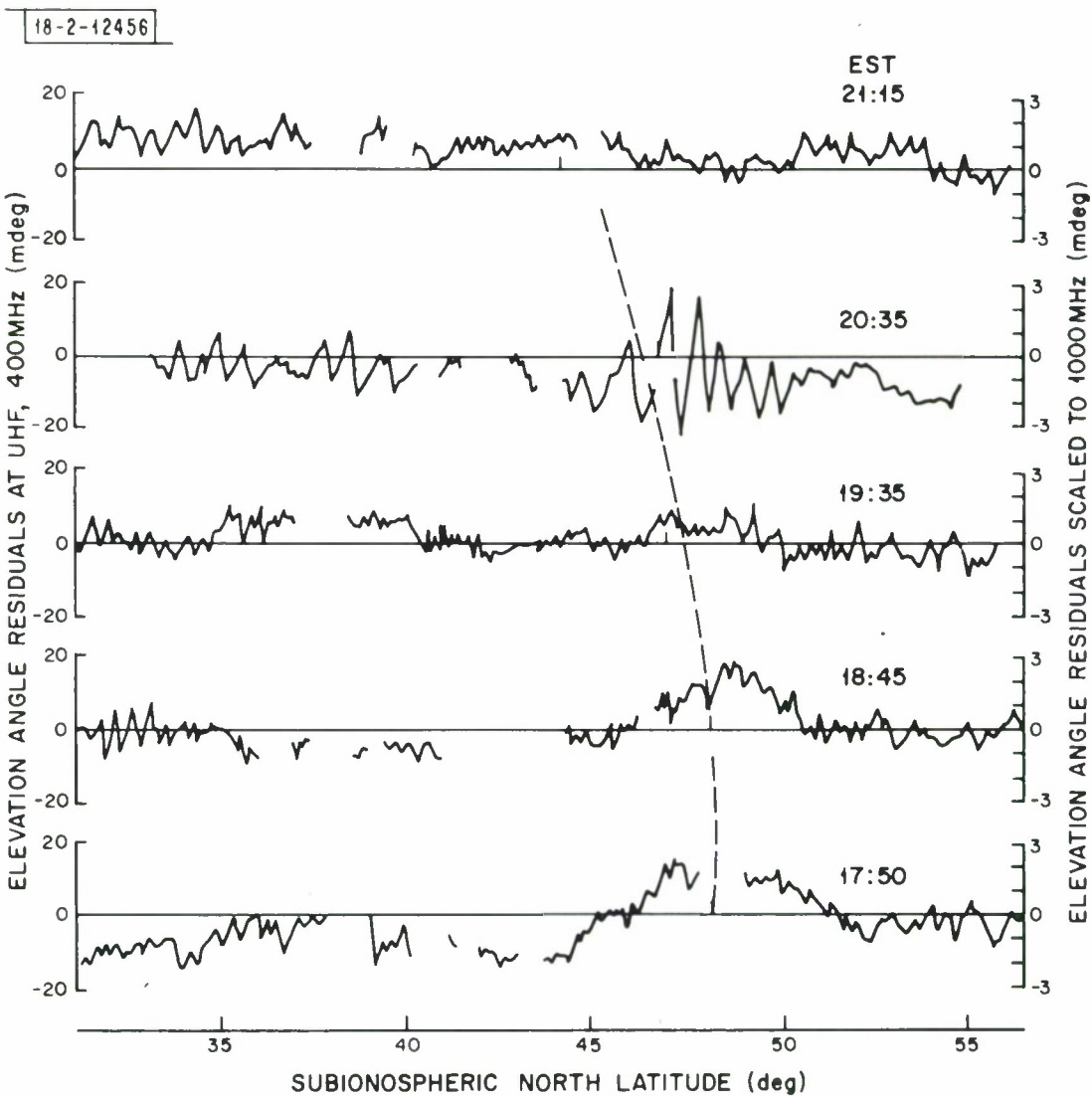


Fig. 19b Successive records on 28 November 1972, (passes of the Navy Navigation Satellites) exhibiting tracking perturbations in UHF elevation angle introduced by the presence of the high-latitude trough. Dashed line marks the location of the peak differential-doppler excursion.

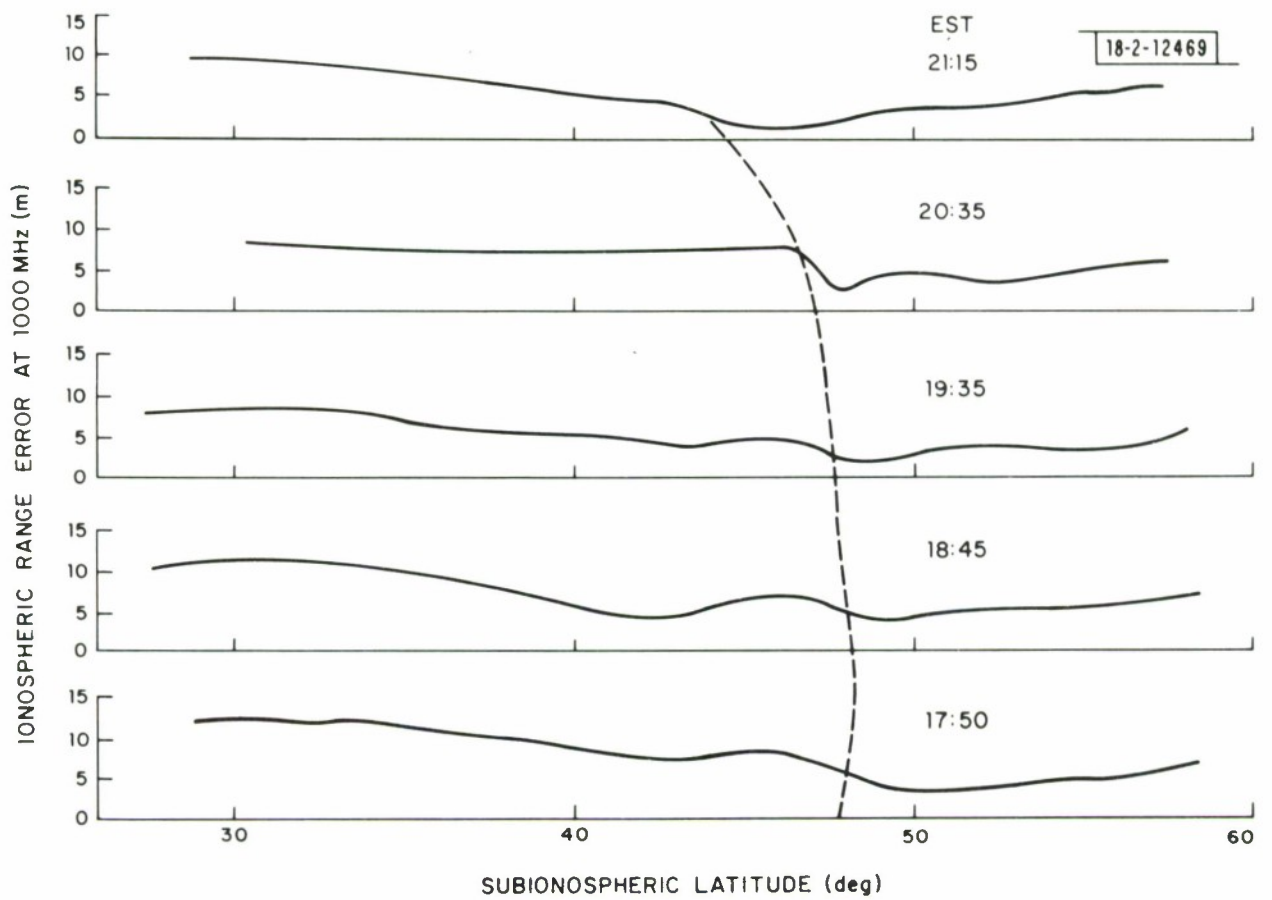


Fig. 19c Successive records on 28 November 1972, (passes of the Navy Navigation Satellites) showing the range error at 1000 MHz introduced by the presence of the high-latitude trough. Dashed line marks the location of the peak differential-doppler excursion.

at $f = 1000$ MHz derived from equation 18 and the differential-doppler results in Figure 19a. For this example the trough has caused range errors about 5 m less than would have been produced by the ambient ionosphere in the absence of the trough. From the largest trough-induced differential-doppler perturbation observed during the Millstone study, we estimate the maximum range error would be about -10 m.

VI. TID - INDUCED ERRORS

Large scale electron density perturbations in the F-region of the ionosphere have been observed by a number of different techniques. These wavelike electron density fluctuations characteristically possess a horizontal component of velocity and are referred to as traveling ionospheric disturbances (TIDs). TIDs are believed to result from internal atmospheric gravity waves which propagate in the neutral gas and produce compression and rarefaction of the electron gas. Wave periods from minutes to hours and horizontal wavelengths from tens to thousands of kilometers have been observed. The slowly-varying angle and range biases produced by TIDs can degrade a radar system's ability to locate a target and predict its future position.

It is expected that the approximations of geometrical optics will apply for propagation through TIDs so that angle and range errors will scale inversely as radar frequency (f) squared. For the purpose of this study, free use is made of TID results obtained at UHF by applying the f^{-2} scaling factor to extrapolate to L-band.

The experimental study conducted at Millstone Hill (Section II) demonstrated some of the propagation effects produced by TIDs. TID-induced fluctuations in differential-doppler and elevation angle were evident in many of the satellite tracks observed at Millstone Hill, and an example is shown in Figure 20. The fluctuations in traverse angle were generally smaller than in elevation angle (Figure 20).

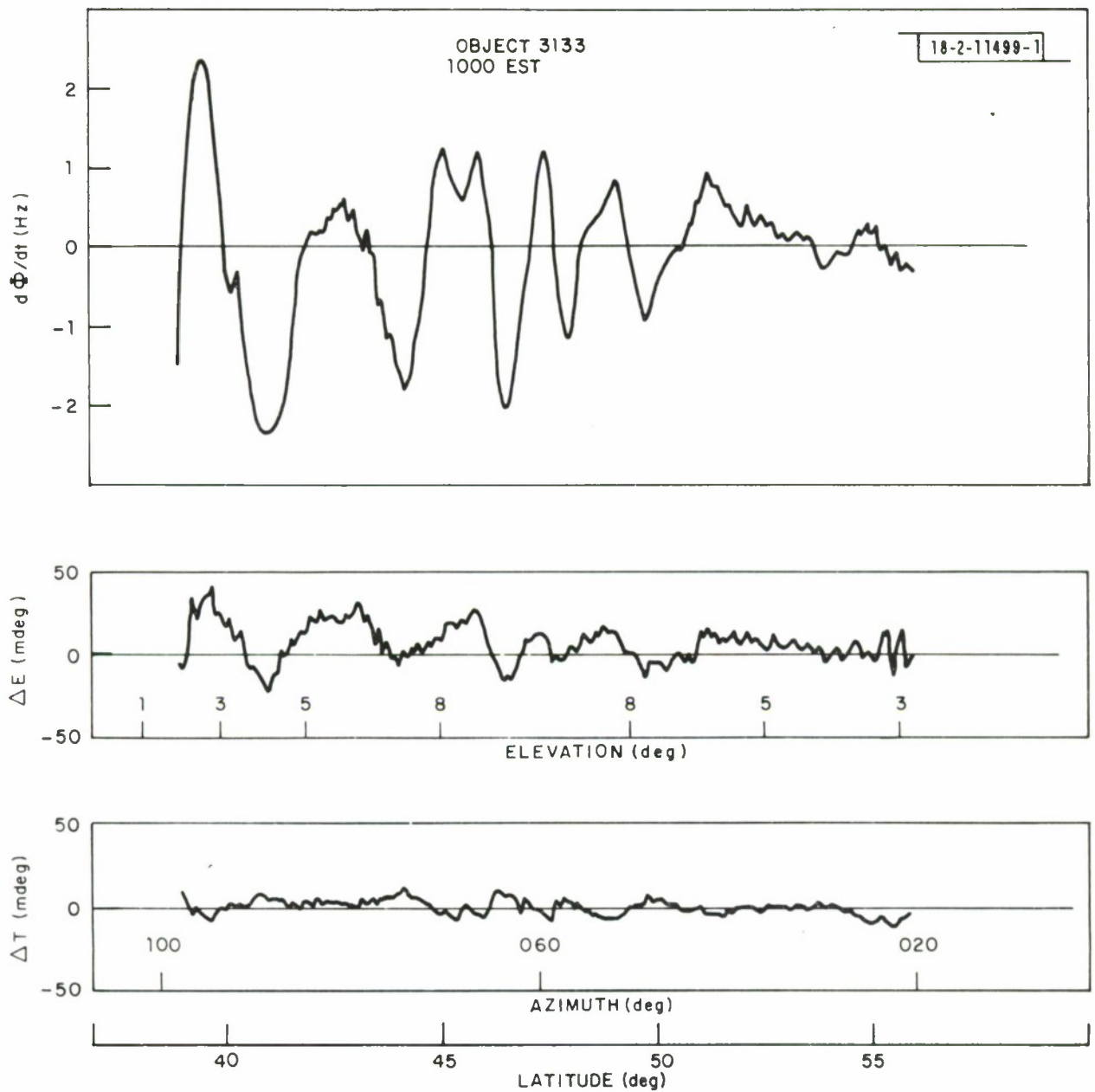


Fig. 20 Example of correlated differential-doppler and elevation error perturbations at UHF obtained from the Millstone Hill propagation study.

A statistical study of the occurrence and amplitude of TIDs was based on the differential-doppler data recorded over the two year period of the Millstone Hill satellite tracking program. The rapid motion of the satellite ensured that the time for the radar line-of-sight to traverse a TID wavelength was shorter than the TID period, so that the differential-doppler records revealed the horizontal spatial structure of a TID, but gave no information on its period. For each TID, the wavelength, amplitude and latitude at the peak differential-doppler excursion were scaled from the tracking records, and used to construct the histograms shown in Figures 21, 22, 23 and 24.

There was a marked diurnal variation in the occurrence of TIDs with a maximum during the daytime (Figure 21). A partial explanation of this effect is that the electron density fluctuations produced by a given gravity wave are proportional to the ambient electron density, which is smaller at night.

The geographic distribution of TIDs (Figure 22) shows a strong peak to the south of Millstone Hill, although some TIDs are observed to the north. The phase fronts associated with a TID are tilted in the direction of travel and anomalous propagation effects are most pronounced when the direction of propagation is aligned along a phase front. Thus, the peak in occurrence to the south is interpreted as evidence that most TIDs seen at Millstone Hill are produced by southward propagating gravity waves. This indicates a generation mechanism to the north, possibly in the auroral zone. TID-induced angle fluctuations were observed mainly in elevation rather than in azimuth, which is further evidence that the TID wavefronts are oriented E-W rather than N-S.

Figure 23 shows a peak in the wavelength distribution of TIDs near 250 km. The detailed shape of the wavelength distribution may be partly due to observational biases, but the rapid fall off at short wavelengths is apparently a true effect for differential-doppler fluctuations produced by TIDs. However, TIDs of shorter wavelengths are still present and they can produce elevation angle fluctuations, as discussed later. The wavelength distribution in Figure 23 can be reasonably represented as,

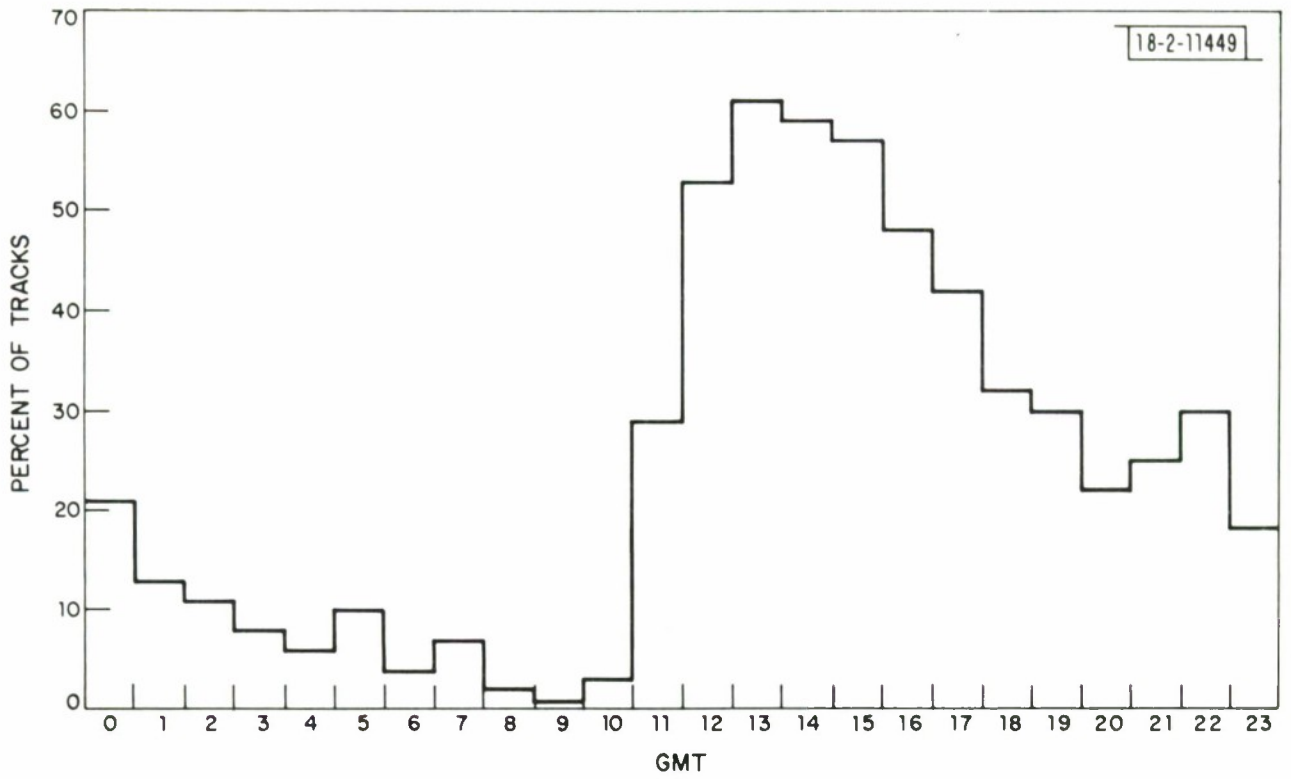


Fig. 21 Percentage of tracks exhibiting TIDs in the differential-doppler records gathered at Millstone Hill between January 1971 and March 1973 vs time of day.

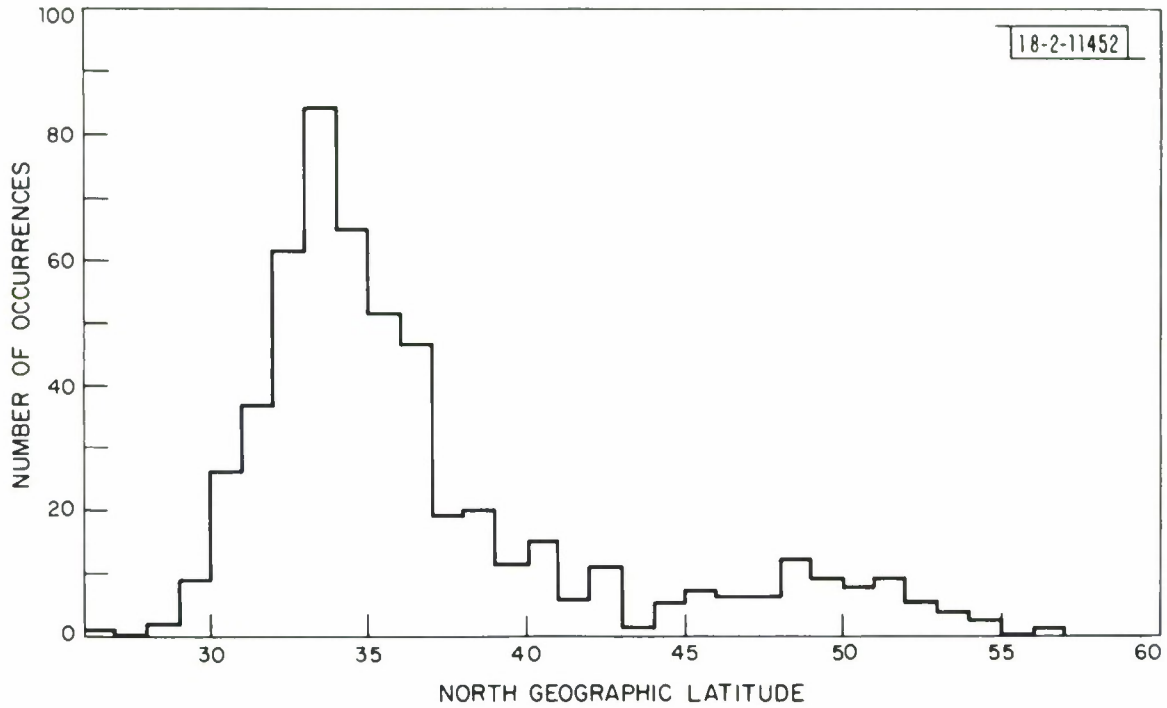


Fig. 22 Number of tracks exhibiting TIDs in the differential-doppler records gathered at Millstone Hill between January 1971 and March 1973 vs latitude.

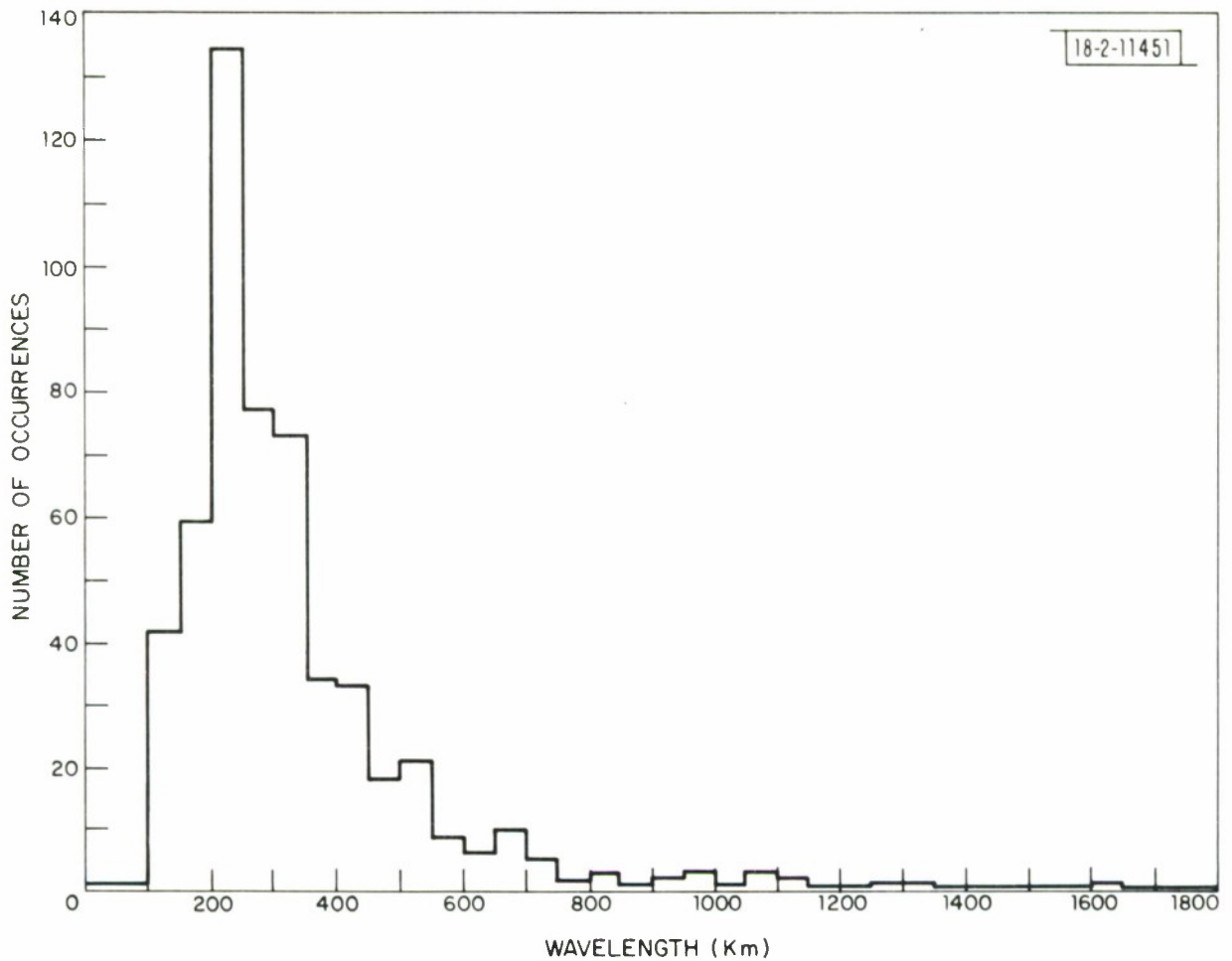


Fig. 23 Number of tracks exhibiting TIDs in the differential-doppler records gathered at Millstone Hill between January 1971 and March 1973 vs TID wavelength.

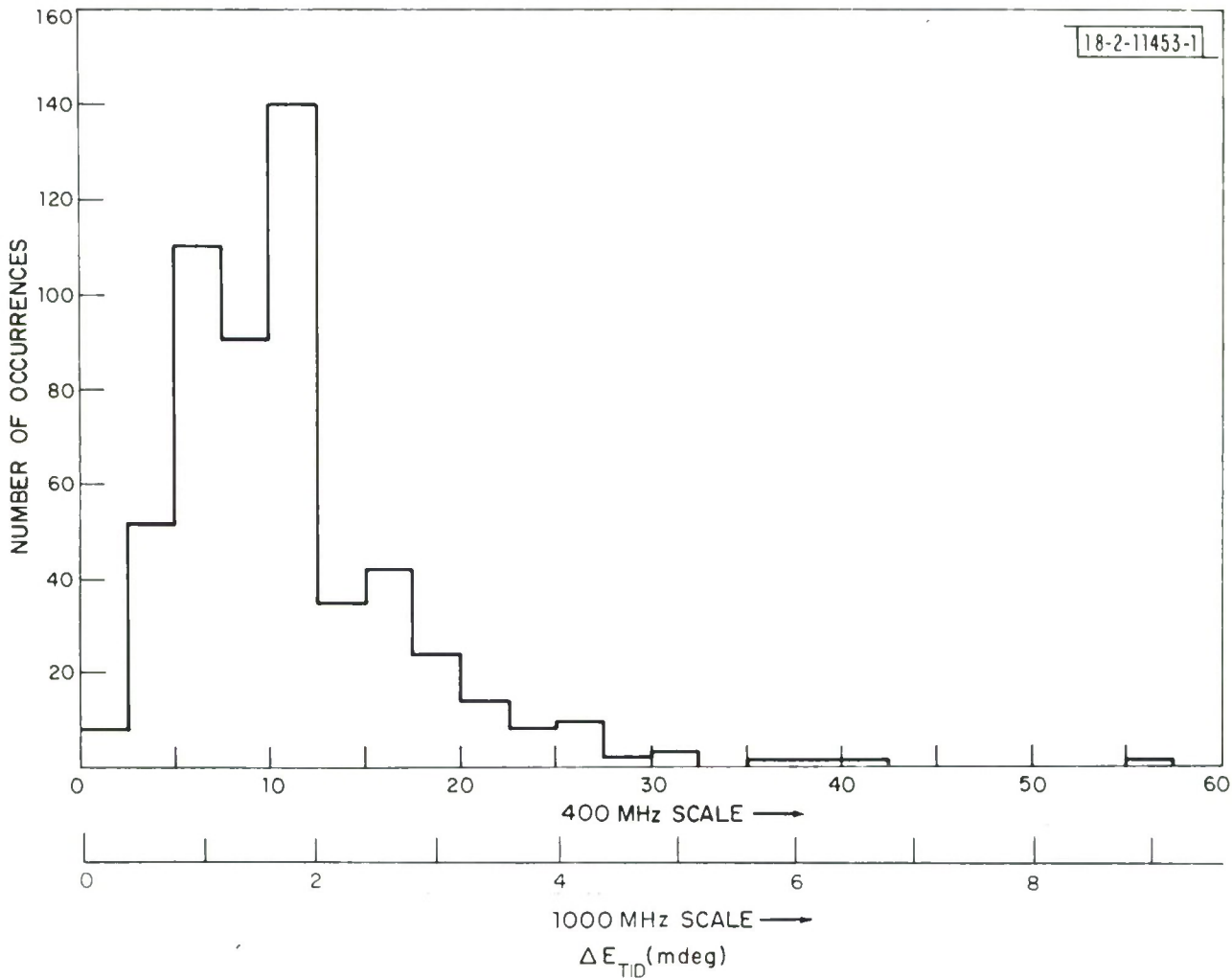


Fig. 24 Number of tracks exhibiting TIDs in the differential-doppler records gathered at Millstone Hill between January 1971 and March 1973 vs TID amplitude. The amplitude has been converted to equivalent elevation angle amplitude at UHF (peak-to-peak) using a scaling law of 10 mdeg/Hz.

$$\begin{aligned} \% \text{ of TIDs with wavelength exceeding } \lambda (\text{km}) &= 100 \exp \left[-(\lambda/350)^2 \right] \\ \lambda &\geq 100 \text{ km} \end{aligned} \quad (19)$$

The satellite tracking data were also analyzed to determine the ratio of the amplitudes of the TID-induced fluctuations in elevation angle and differential-doppler. The resulting average value was near 10 mdeg/Hz, and was similar to values predicted by ray-tracing studies using TID models.⁴ With this scaling factor the measured distribution of TID amplitudes from the differential-doppler records was converted to elevation angle and scaled to a frequency of 1000 MHz. Figure 24 gives the resulting amplitude distribution for the 20% of the satellite tracks for which TIDs were observed; ΔE_{TID} denotes the peak-to-peak amplitude of the TID-induced fluctuation in elevation angle. The distribution in Figure 24 (for a 1000 MHz operating frequency) is approximately given by,

$$\begin{aligned} \% \text{ of TIDs with peak-to-peak amplitude exceeding } A(\text{mdeg}) &= 100 \exp \left[- (A/2)^2 \right] \\ \lambda &\geq 100 \text{ km} \end{aligned} \quad (20)$$

The radar range error and the differential-phase angle introduced by the ionosphere are both proportional to the total electron content along the radar line-of-sight to the satellite, as given in equation 18. An example of range errors calculated from differential-doppler data via equation 18 is shown in Figure 25, along with the measured UHF elevation error scaled to 1000 MHz. In this example, there are TID-induced range errors of 4 m peak-to-peak and elevation errors of 10 mdeg peak-to-peak, which are superimposed on the values produced by the ambient ionosphere.

Ray-tracing studies using TID models⁴ give the approximate relationship between the amplitudes of TID-induced range and elevation errors (in m and mdeg, respectively) as,

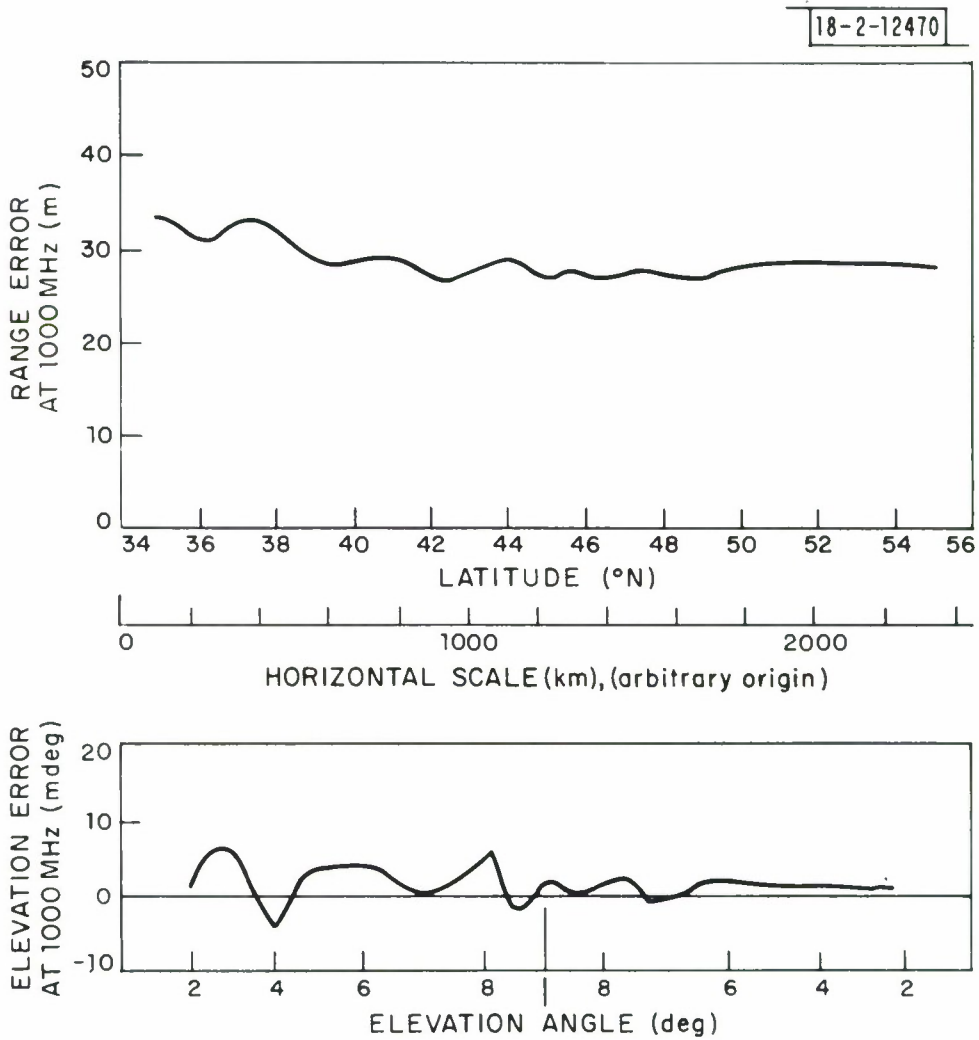


Fig. 25 Example of TID-induced elevation and range errors (scaled to 1000 MHz) from Millstone Hill satellite tracking record.

$$\frac{\Delta E_{\text{TID}}}{\Delta R_{\text{TID}}} \approx \frac{700}{\lambda_{\text{TID}}} \text{ mdeg/m} \quad (21)$$

$$100 < \lambda_{\text{TID}} < 2000 \text{ km}$$

where λ_{TID} is the TID wavelength in km.

The approximate amplitude distribution of range errors produced by TIDs may be obtained by combining equations (21) and (20). Equation (21) indicates that range errors may become less important than elevation errors for short wavelength TIDs.

Predictive schemes may be used to correct for most of the radar range errors and angle biases produced by the ambient ionosphere depending on how accurately f_m is estimated (Section III and IV). However, TID-induced errors cannot be predicted for an individual radar track as, at best, only probability of occurrence can be specified. One real-time corrective scheme for range error involves simultaneous radar measurements of propagation time at two different frequencies. The possible presence of TID-induced range errors places a limit on how reliably range error, determined in this way, can be extrapolated to other points along the track or to other nearby objects, as the TID-induced range error may change sign for penetration points with a horizontal separation of $\lambda_{\text{TID}}/2$. The problem of TID-induced errors is of most concern in the daytime for a radar situated below the auroral zone and looking southward.

The TID characteristics discussed so far apply to wavelengths above 100 km, as TIDs of shorter wavelengths apparently did not produce differential-doppler signatures. The cutoff at short wavelengths displayed by the differential-doppler data was not present in TID-induced elevation angle fluctuations, as was evident from the UHF beacon tracking results. In this study the UHF traverse and elevation angle fluctuations were determined by comparing three-sec averages with 63-sec running averages along the satellite track. The smoothing process effectively limited the range of TID wavelengths which could be studied to between 20 and 150 km. The angle

fluctuations detected in this way were confined mainly to elevation, and an example is shown in Figure 26, scaled to an operating frequency of 1000 MHz.

The elevation angle fluctuations are often almost sinusoidal in character (as in Figure 26), but sometimes appear to be the mixture of a number of different wavelengths. In order to characterize the TID amplitude in an objective way, the equivalent peak-to-peak amplitude (ΔE_{TID}) was calculated as $2\sqrt{2}$ x rms elevation angle fluctuation, as would apply for a purely sinusoidal oscillation. The mean TID amplitude ($\overline{\Delta E}_{\text{TID}}$) obtained by averaging over all satellite tracks is shown as a function of elevation angle in the lower part of Figure 27, both for looking south and looking north. In contrast with the larger wavelength TIDs observed in the differential-doppler study, there is little tendency for more short wavelength TIDs in the south than in the north. This argues for a different generation mechanism for these TIDs which is not associated with the auroral zone.

The diurnal variation of mean TID amplitude (scaled to 1000 MHz) is presented in the upper part of Figure 27. The maximum mean amplitude occurs in the daytime, as with longer wavelength TIDs, and the explanation again may be the controlling influence by the diurnal variation in ambient electron density.

The distribution of the peak-to-peak amplitude of the short wavelength TIDs is shown in Figure 28. All satellite tracks were included in this analysis, rather than just those exhibiting recognizable TID-induced elevation errors.

VII. IONOSPHERIC SCINTILLATION

A. General

Observations by means of a variety of techniques have shown that small-scale irregularities in the ionization concentration (and hence refractive index) are a normal feature of the ionosphere. There is a marked variation in the incidence of irregularity structure over the globe with the maximum rate of occurrence and intensity in the equatorial zone at night and in the polar and auroral zones. In addition to latitudinal and diurnal variations, the occurrence of irregularities is correlated with season, sunspot

18-2-12457

OBJECT 2807
TIME 0522
GMT DAY 104
YEAR 72
TRACK 210406

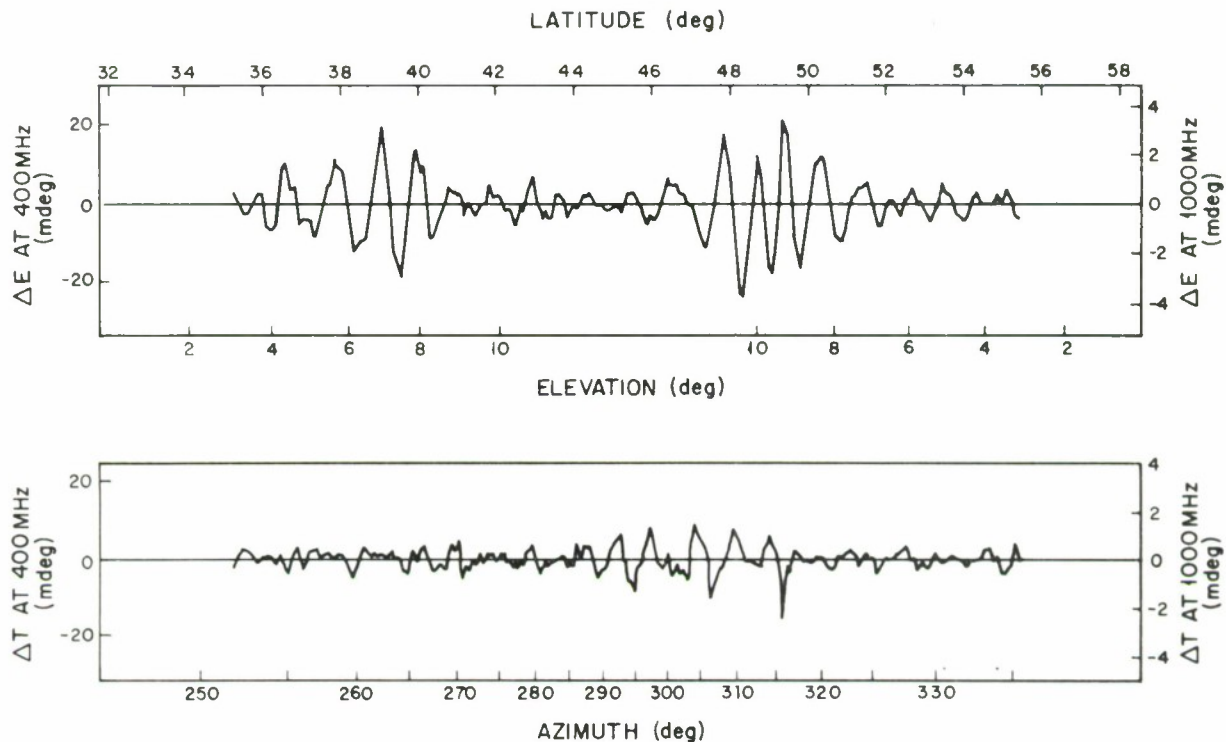


Fig. 26 Example of elevation and traverse angles measured by the Millstone Hill UHF satellite beacon tracker. Angles were computed as a 3-sec mean value referenced to 63-sec mean value.

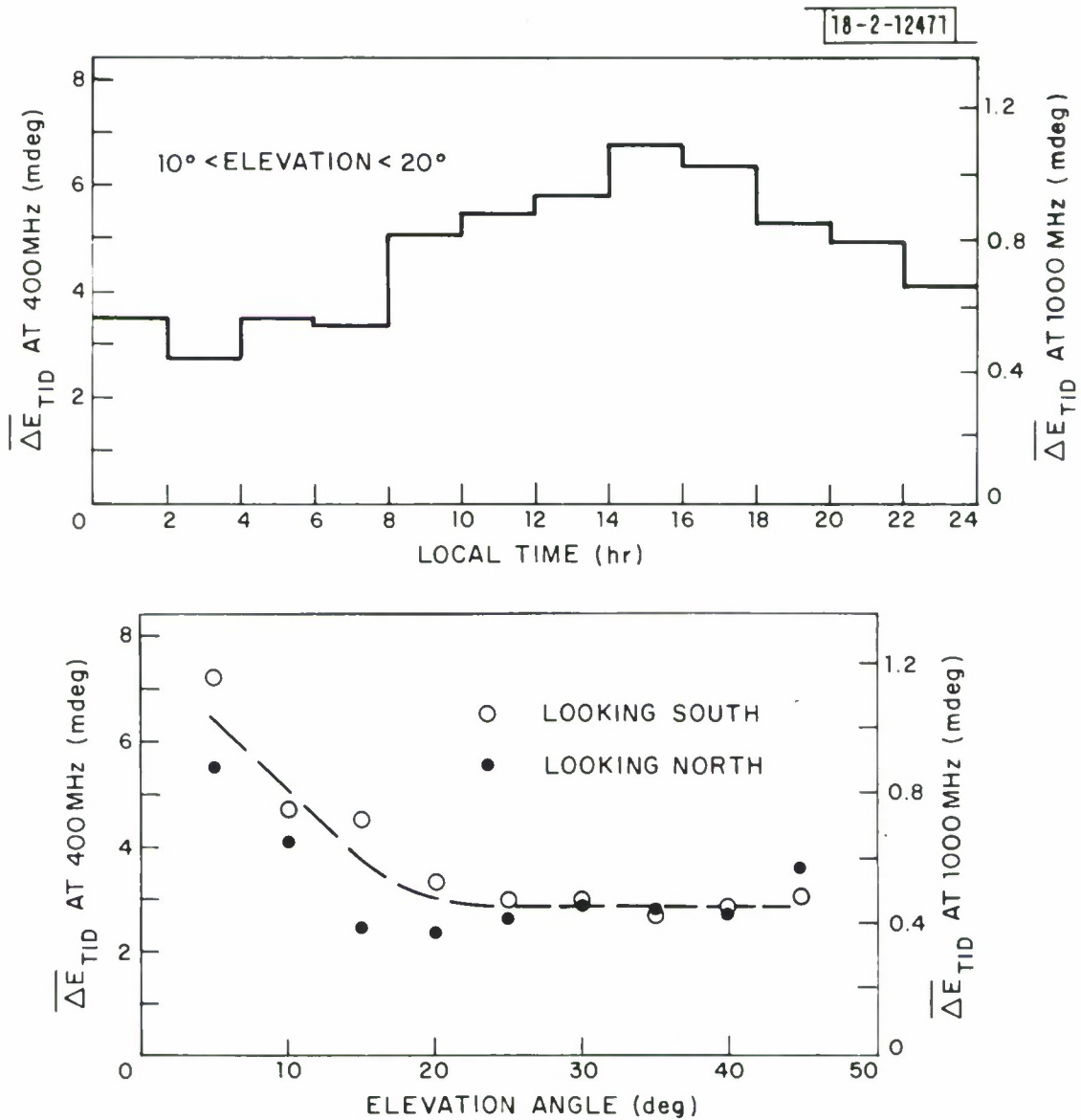


Fig. 27 Local time dependence (upper part) and elevation angle dependence (lower part) of the mean peak-to-peak amplitude of elevation angle fluctuations induced by short wavelength TIDs. The mean was obtained by averaging over all the UHF beacon tracker records (Figure 26) gathered at Millstone Hill from January 1971 to March 1973.

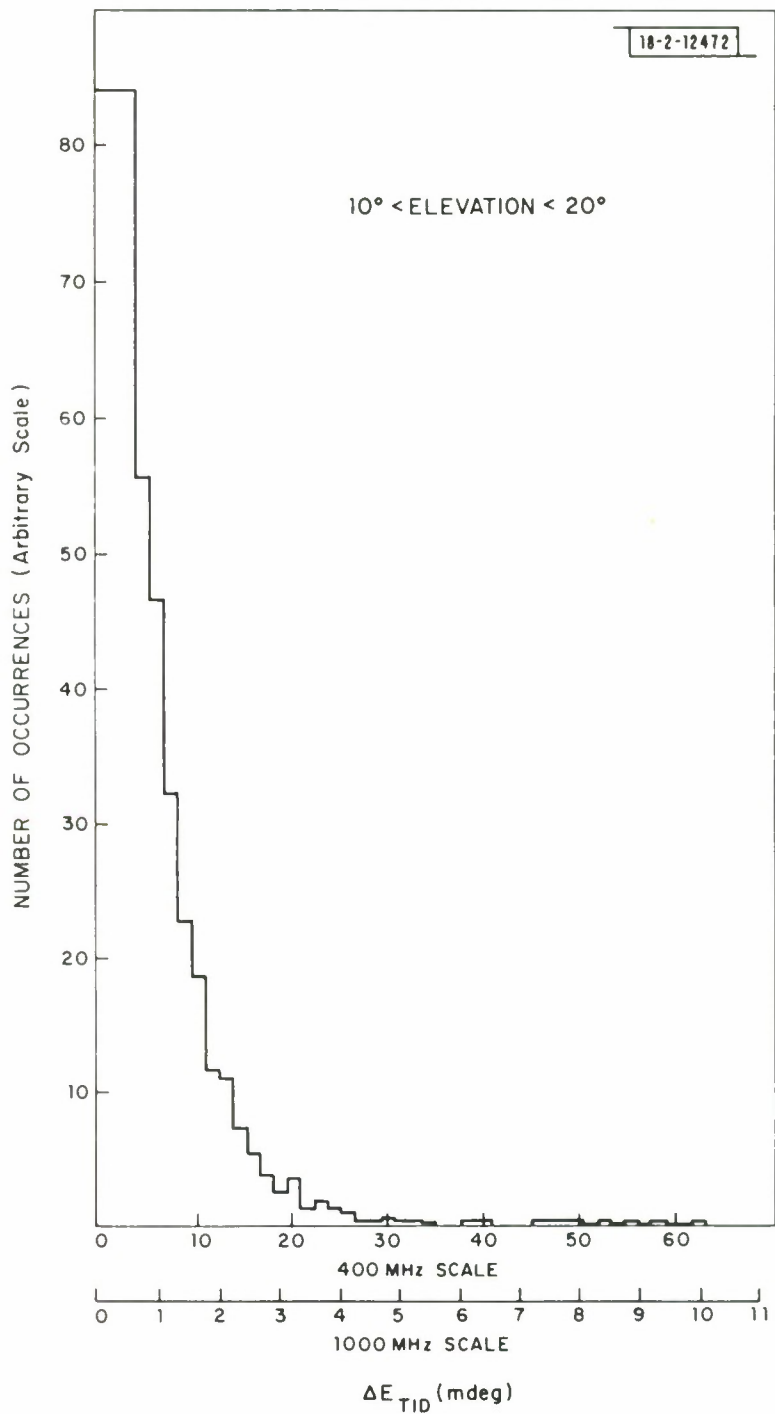


Fig. 28 Distribution of peak-to-peak amplitude of elevation angle fluctuations produced by short wavelength TIDs, as observed in the Millstone UHF beacon tracker records gathered from January 1971 to March 1973.

number and magnetic activity.

The fluctuations imposed on radio waves which are scattered by the irregularities are called scintillations and are present in amplitude, phase and angle-of-arrival of the received radio wave. The irregularities causing scintillation of signals above VHF are almost entirely confined to the F-region and are elongated along the geomagnetic field. Scintillation effects tend to decrease with increasing frequency, but the simple f^{-2} scaling law appropriate to geometric optics is not necessarily applicable to scintillation.

A study of scintillation in the auroral zone was undertaken using the UHF (400 MHz) amplitude and angle data collected on over 2300 satellite beacon tracks conducted for the Millstone Hill propagation study (Section II). The results of this study allowed models to be constructed giving the occurrence of scintillation as a function of invariant latitude (42° - 70° N), local time, geomagnetic activity (K_p) and season, although the model could still only strictly be applied to the sunspot conditions prevailing when the observations were made (1971-1973). The models were extended to L-band by employing frequency scaling laws based on an assumed three-dimensional power-law wavenumber spectrum of electron density fluctuation with an exponent of -4.

B. Elevation Angle Dependence of Scintillation

The manner in which the scintillation index varied along a satellite track was a combination of a true spatial change in the irregularity characteristics and effects produced by the changing geometry along the track. For a uniform layer of irregularities at a fixed height, the scintillation index increases as the elevation angle is lowered because of the increasing thickness of the irregularity layer along the propagation path, and also because the observer moves further from the irregularities. If these purely geometrical effects are corrected for, then the true latitudinal dependence of the scintillation index and irregularity characteristics may be studied.

The elevation scaling law for the scintillation index was determined directly from the Millstone Hill satellite tracking results. This was possible because the wide variety of satellite tracking geometries, which were used in the study, permitted observations at the same invariant latitude for a range of different elevation angles. In each 2° interval of invariant latitude, the mean scintillation index was determined as a function of elevation angle and used to calculate the elevation correction factor. The results are shown in Figure 29 along with the theoretical curve for a power-law irregularity spectrum with a three-dimensional spectral index of minus four. This type of irregularity spectrum predicts the observed elevation dependence quite well and explains many other characteristics of ionospheric scintillation observed at Millstone Hill and elsewhere⁷. Based on the elevation scaling law shown in Figure 29 all the measured scintillation indices were converted to the standard case of a transmitter at an infinite distance in the zenith. This procedure removed any dependence of the results on the particular latitude at which the observations were made and the height of the satellite beacon which was tracked.

The ionospheric irregularities producing scintillation are elongated along the earth's magnetic field and the scintillation index depends on the elongation ratio α and the propagation angle ψ (angle between propagation direction and magnetic field). Thus, the results should be normalized to some reference value of ψ , as well as a reference elevation angle. However, the dependence of S on ψ and α is not strong provided that $\psi > 30^\circ$, a condition which is satisfied by most of the Millstone Hill satellite tracks, and it was sufficiently accurate to ignore the elongation of the irregularities in normalizing the observations of scintillation index. It should be remembered that the results only strictly apply for observations transverse to the field lines rather than along the field lines.

C. Dependence on Geomagnetic Activity and Season

A statistical analysis of the Millstone Hill tracking results was carried out after correcting the measured scintillation indices for baseline effects and normalizing to a transmitter at infinity in the zenith.

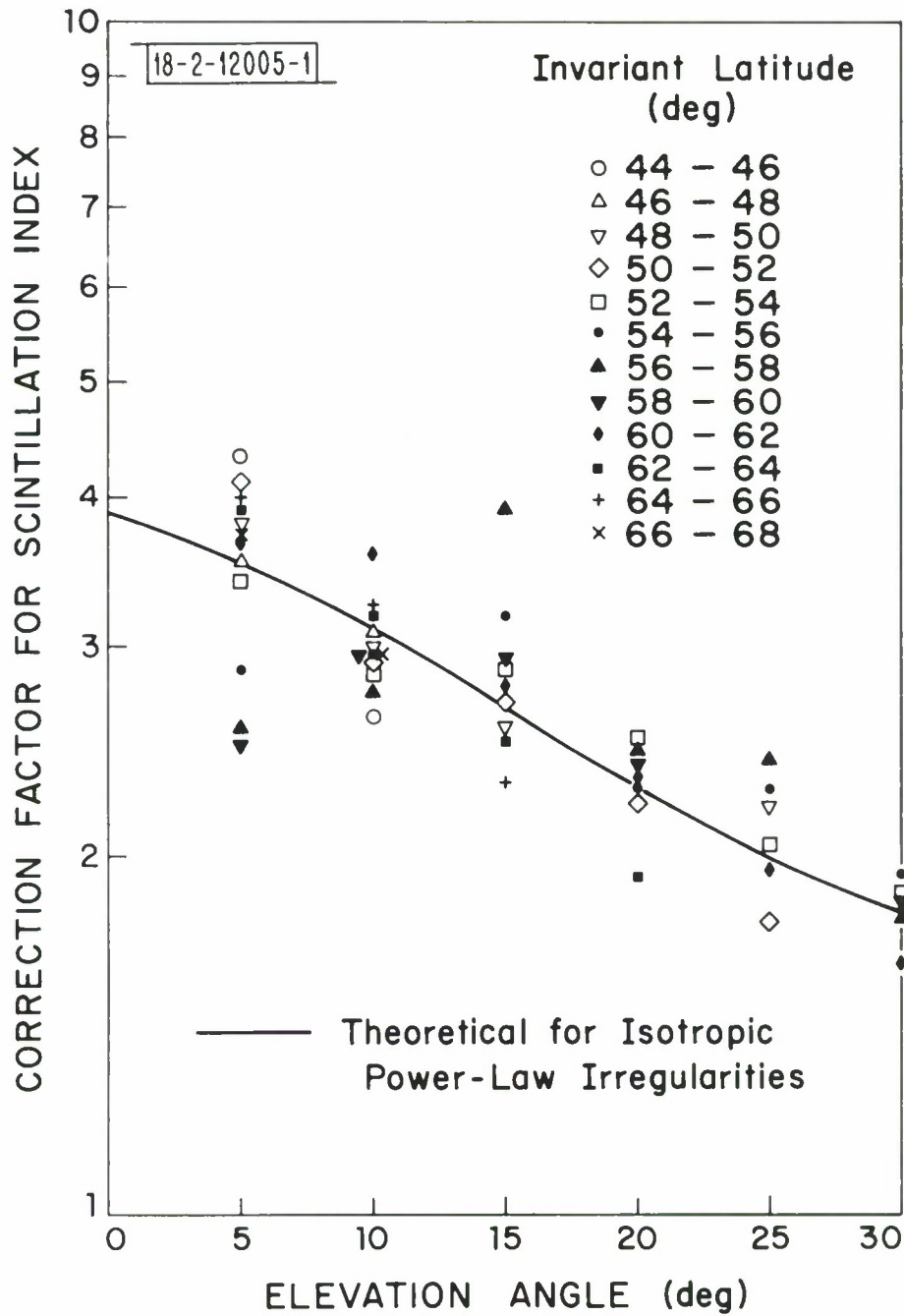


Fig. 29 Elevation dependence of scintillation index from Millstone Hill satellite tracking data.

The data were divided into three levels of geomagnetic activity (quiet, K_p from 0_0 to 1_+ ; moderate, K_p from 2_- to 3_+ ; and disturbed, K_p from 4_- to 5_+) and two seasons (summer and winter, defined between equinoxes). For each two hour interval of local time and 2° interval of invariant latitude, the mean scintillation index was calculated and used to construct contour plots. The results are given in Figures 30a to 30f for the different K_p levels and seasons.

In general, scintillation activity is confined to invariant latitudes above 55° and increases with increasing K_p . Some quite marked seasonal differences are also evident. In summer the mean scintillation index is a maximum around local time 20 to 02 hours, whereas in winter the maximum occurs around 14 to 20 hours, i.e., about six hours earlier.

D. Scintillation Boundary

The scintillation boundary is defined as the equatorward edge of F-region irregularity structure in the auroral zone which causes scintillation of UHF-VHF radio waves^{8,9}. The present observations on occasion show a rapid increase in scintillation at high latitudes which is characteristic of a sharp boundary (see Figure 2 for example), but more often the increase is more in the nature of a gradual onset of scintillation activity. A scintillation boundary can be defined from the present statistical analysis in an objective way by designating a particular (but arbitrary) value of the mean scintillation index to represent a boundary level. Figures 31a and 31b show the scintillation boundaries which result from selecting a mean scintillation index of 0.02 as a boundary value.

The seasonal dependence of scintillation is clearly evident in the position of the scintillation boundary shown in Figures 31a and 31b. There is a southward progression of the boundary with increasing K_p , which is especially marked in the midnight sector in winter and the early morning sector in summer. This picture of the scintillation boundary is somewhat dependent on the particular mean value of scintillation index selected as a boundary value.

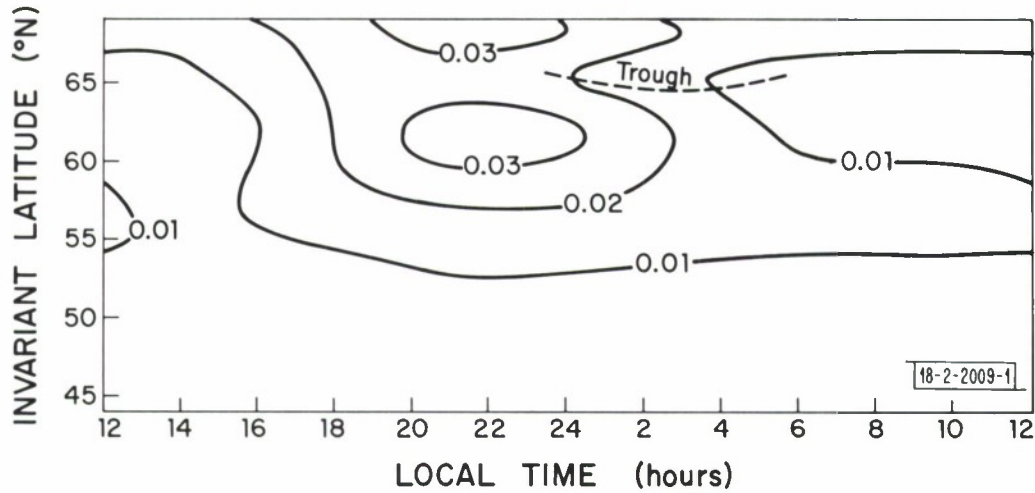


Fig. 30a Contours of mean scintillation index at 400 MHz (normalized to zenith) from Millstone Hill satellites tracking observations 1971-1973, for summer with K_p from 0_o to 1_+ .

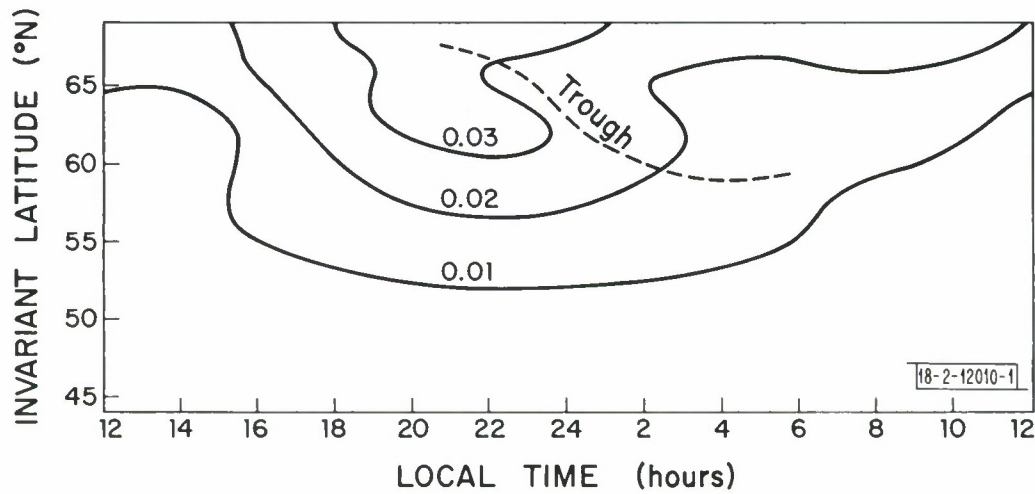


Fig. 30b Contours of mean scintillation index at 400 MHz (normalized to zenith) from Millstone Hill satellite tracking observations 1971-1973, for summer with K_p from 2_- to 3_+ .

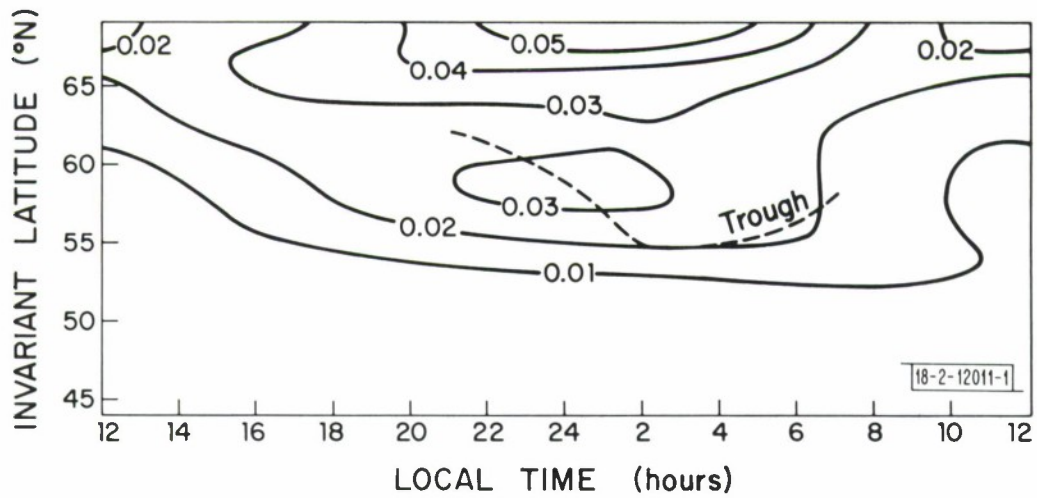


Fig. 30c Contours of mean scintillation index at 400 MHz (normalized to zenith) from Millstone Hill satellite tracking observations 1971-1973, for summer with K_p from 4_- to 5_+ .

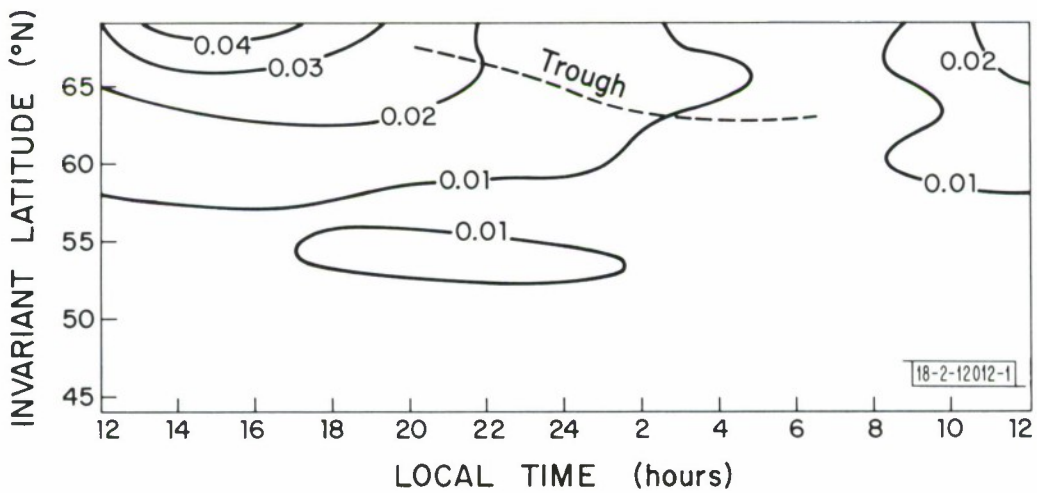


Fig. 30d Contours of mean scintillation index at 400 MHz (normalized to zenith) from Millstone Hill satellite tracking observations 1971-1973, for winter with K_p from 0_0 to 1_+ .

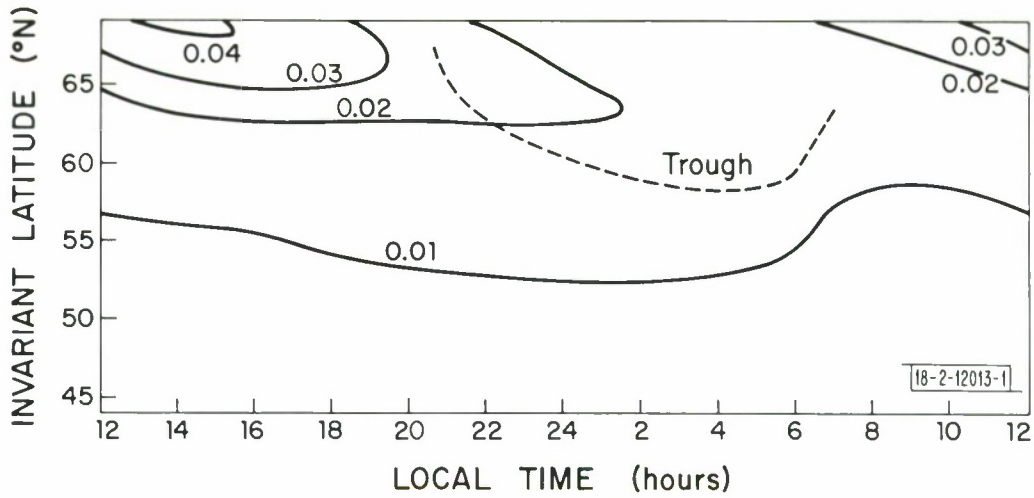


Fig. 30e Contours of mean scintillation index at 400 MHz (normalized to zenith) from Millstone Hill satellite tracking observations 1971-1973, for winter with K_p from 2_- to 3_+ .

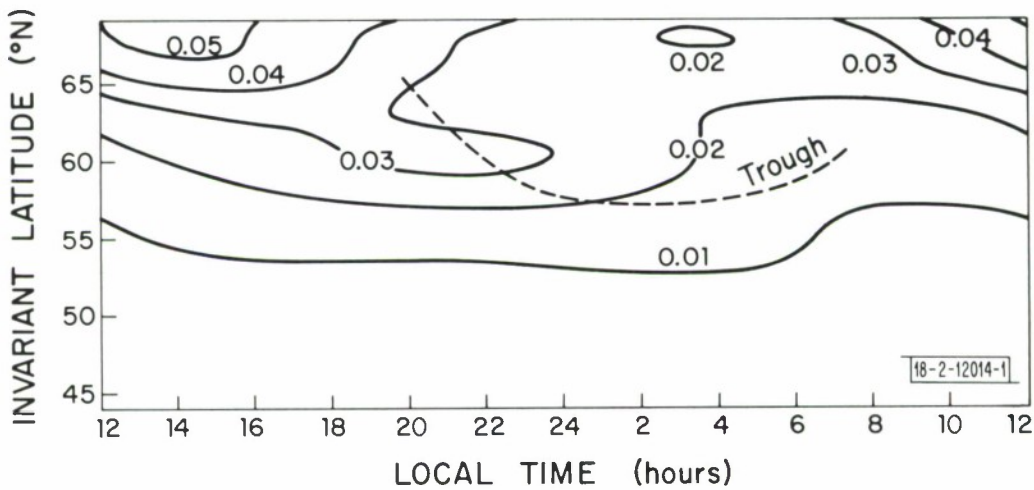


Fig. 30f Contours of mean scintillation index at 400 MHz (normalized to zenith) from Millstone Hill satellite tracking observations 1971-1973, for winter with K_p from 4_- to 5_+ .

- Kp 0₀ to 1₊
- - - Kp 2₋ to 3₊
- Kp 4₋ to 5₊

18-2-12007-1

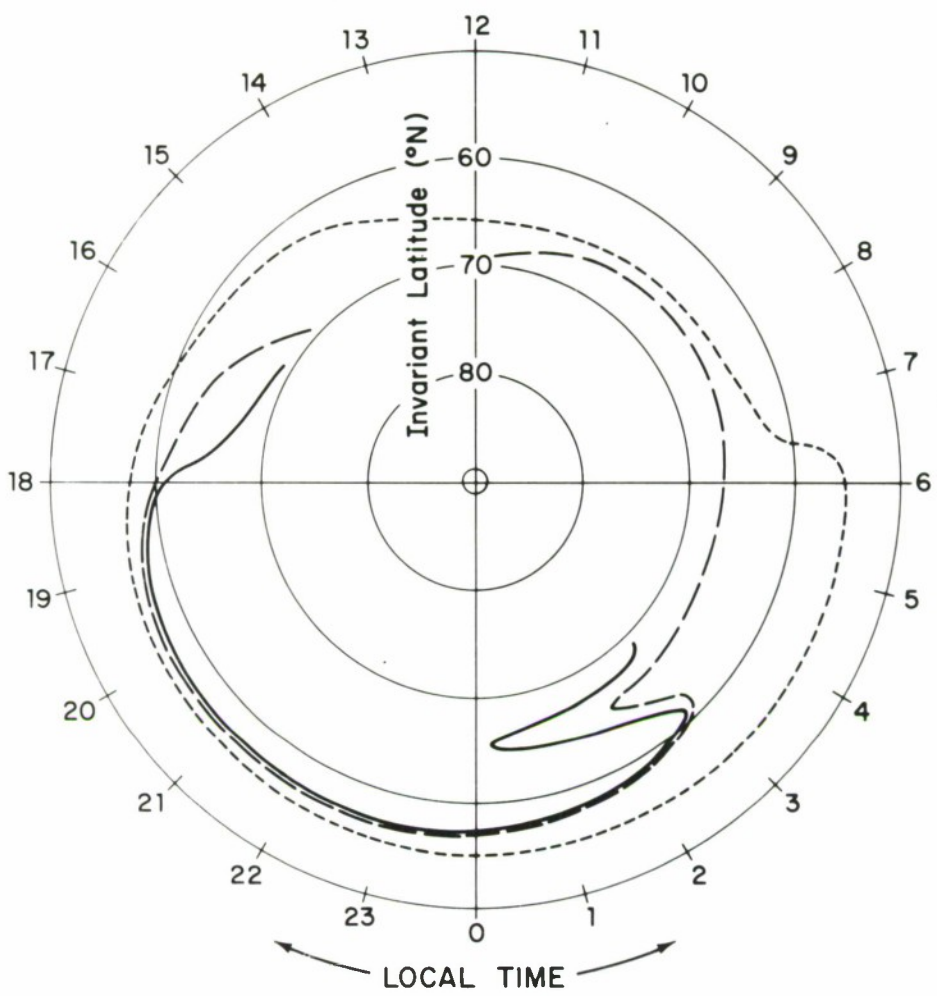


Fig. 31a Positions of the scintillation boundary in winter for three K_p intervals. The boundary is defined by a mean scintillation index of 0.02 at 400 MHz and vertical incidence.

- Kp 0₀ to 1₊
- - - Kp 2₋ to 3₊
- Kp 4₋ to 5₊

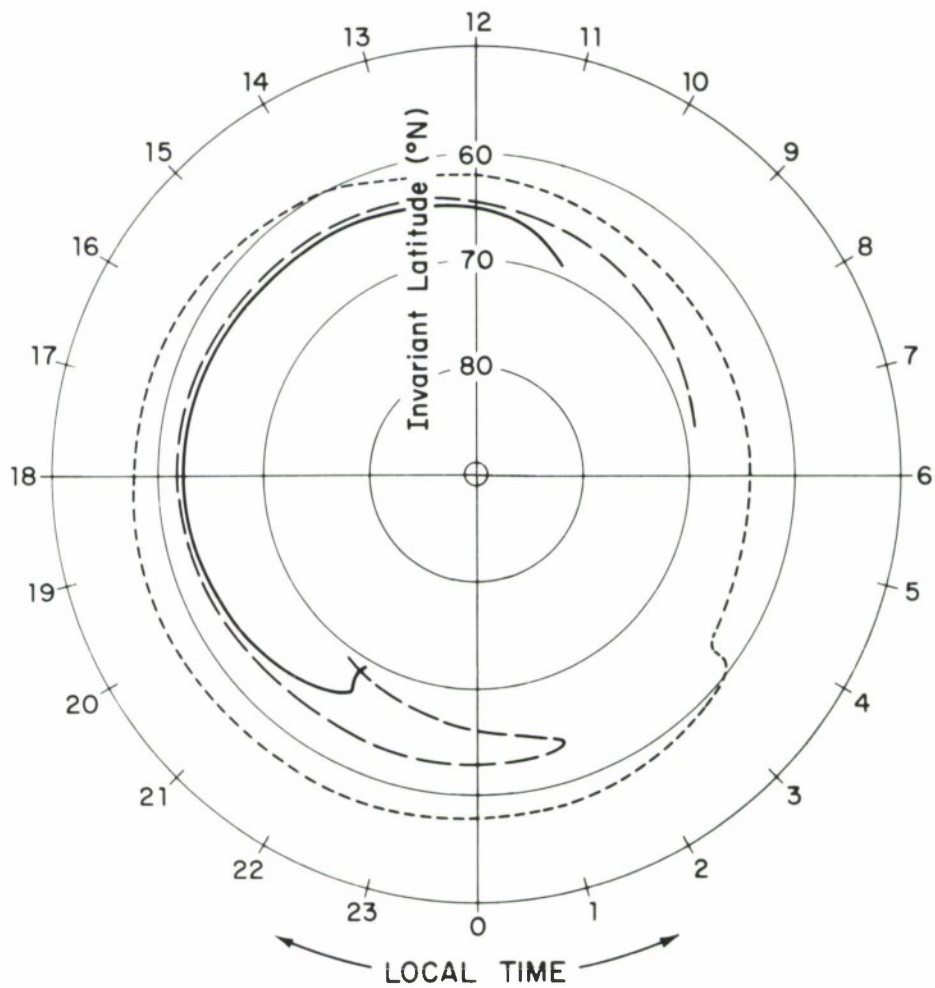


Fig. 31b Positions of the scintillation boundary in summer for three K_p intervals. The boundary is defined by a mean scintillation index of 0.02 at 400 MHz and vertical incidence.

The position of the trough (Section V) is also indicated on the scintillation contour plots in Figures 30a to 30f. No strong correlation between the occurrence of scintillation and the trough position is evident from this comparison.

An analysis of satellite tracks for which both a sharp scintillation boundary and a trough were present simulary showed a lack of correlation in the positions of the two features. Figure 2 provides a good example of this poor correlation.

E. Model for Scintillation Index

The scintillation results may be used to generate a model variation of scintillation index for use in tracking simulation studies where the actual signal amplitude (and angle-of-arrival) is required along the track. The first step is to determine the variation in the mean scintillation index with invariant latitude $\bar{S}(\Lambda)$ along the track for the appropriate local time, K_p , and season (Figures 30a to 30f). The irregularities may be considered to be at a height of 300 km, and Λ is the invariant latitude of the subionospheric point at the penetration point of the irregularities. The variation of \bar{S} calculated in this way represents the average to be expected using a large number of tracks. Figure 32 gives the distribution function for the ratio of scintillation index to mean scintillation index derived from the Millstone Hill tracking data. Thus, a representative track for a particular tracking simulation should be multiplied by a factor M , which is selected on a random basis from a distribution having the form shown in Figure 32. Allowance is made for the particular observing frequency f (in MHz), and elevation angle E using results applicable to the assumed power-law irregularity spectrum and weak-scatter. Thus, the final expression for the model scintillation index is

$$S(\Lambda) = \bar{S}(\Lambda) M \left(\frac{f}{400} \right)^{-\frac{3}{2}} \left(\frac{z}{h_T} \sec i \right)^{\frac{1}{2}} \quad (22)$$

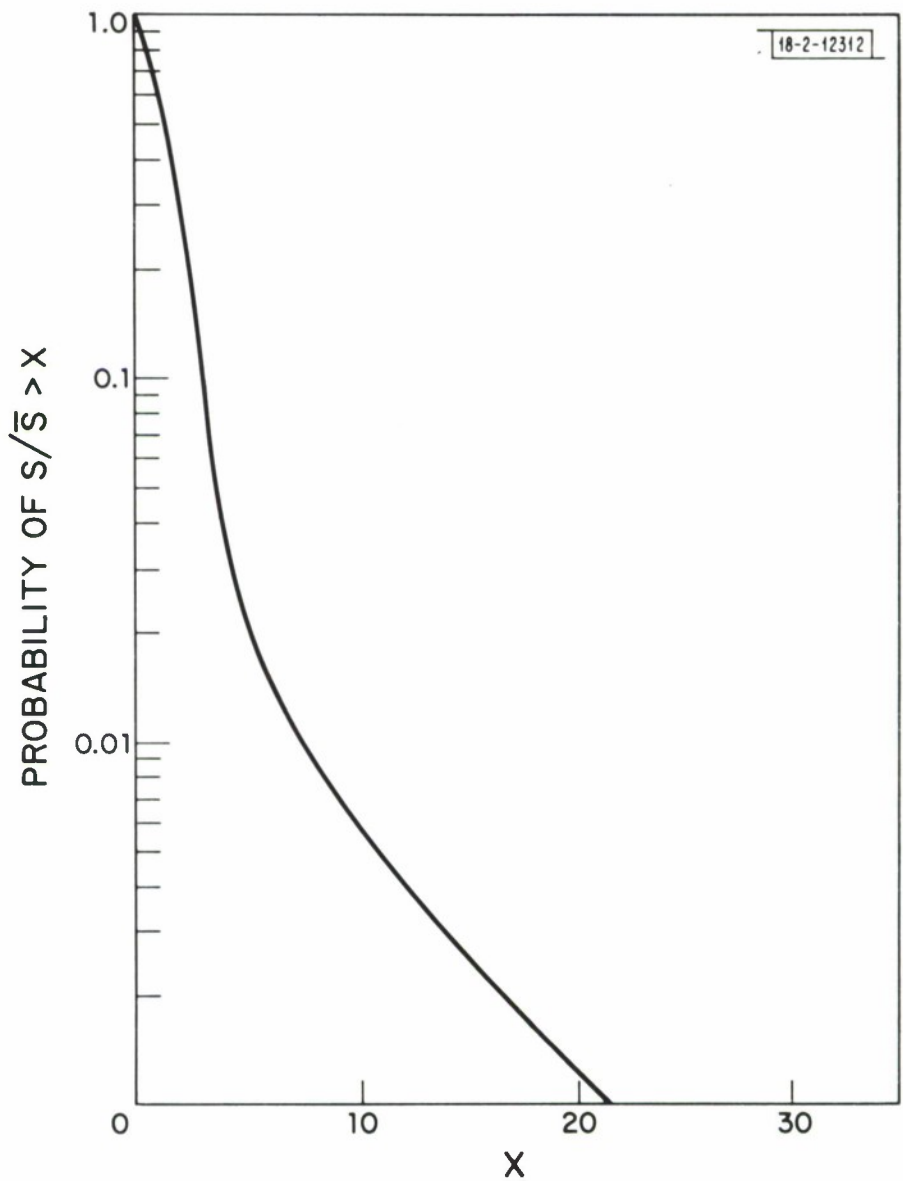


Fig. 32 Probability distribution of scintillation index divided by mean scintillation index, as derived from the Millstone Hill satellite tracking study.

where

$$z = \frac{z_1 z_2}{z_1 + z_2}$$

and the parameters z_1 , z_2 , h_T and i are defined in Figure 33. The zenith angle i at the penetration point of the irregularities is related to the elevation angle by

$$i = \arcsin \left(\frac{r_o \cos E}{r_o + h_T} \right) \quad (23)$$

Equation 22 only applies for $z > 0$, and S should be set to zero once the irregularity layer is penetrated. Physically it is not possible to have S much greater than unity, so if equation 22 gives a value $S > 1$ then we should set $S = 1$.

F. Model for RMS Amplitude Fluctuations

The received amplitude (A) of a radiowave after passing through a layer of ionospheric irregularities will fluctuate about the mean value \bar{A} . The rms fluctuation in relative amplitude $R = A/\bar{A}$ is specified by σ_R ,

$$\sigma_R^2 = \overline{R^2} - 1 = \frac{\overline{A^2} - \bar{A}^2}{\bar{A}^2} \quad (24)$$

The scintillation index S used in the measurements made at Millstone Hill was based on the rms fluctuation in received power relative to the mean, i.e.,

$$S^2 = \frac{\overline{A^4} - \bar{A}^4}{\bar{A}^4} \quad (25)$$

For small fluctuations in amplitude we may convert between the two measures of scintillation using

$$S = 2 \sigma_R \quad (26)$$

Thus the model value of scintillation index effectively yields a value for σ_R via equation 26.

G. Probability Distribution of Amplitude

Theoretical and experimental results indicate that the probability distribution of amplitude fluctuations produced by ionospheric scintillation is satisfactorily represented by the Nakagami m-distribution,

$$f_N(B) = \frac{2m^m B^{2m-1} e^{-mB^2}}{\Gamma(m)} \quad \begin{array}{l} B \geq 0 \\ m \geq \frac{1}{2} \end{array} \quad (27)$$

where B is the amplitude normalized by dividing by the rms amplitude,

$$B = \frac{R}{\left(1 + \sigma_R^2\right)^{\frac{1}{2}}} \quad (28)$$

The parameter m is related to σ_R by $m = (2 \sigma_R^2)^{-2}$

H. Allowance for Radar Case

Once a value of σ_R is calculated from the model, the actual relative amplitude R may be selected on a random basis from a distribution given by equation 27. The relative amplitude so derived applies to a one-way transmission through the irregularities and must be adjusted to the radar situation which involves a two-way transmission. As time from transmission to reception of a radar pulse is much less than the correlation time of the amplitude fluctuations, the conversion to the radar case is accomplished by squaring the relative amplitude. Final conversion to the received radar amplitude (C) is realized by multiplying by the mean value of radar amplitude (\bar{C}), i.e., the amplitude if no scintillations were present. Thus

$$C = R^2 \bar{C} \quad (29)$$

I. Correlation Time of Amplitude Fluctuations

The fluctuations in amplitude and angle-of-arrival at a receiver arise either because the ionospheric irregularities are changing with time, or because the diffraction pattern is moving past the receiver due to motion

of the source or the irregularities. The effects due to change in the ionosphere are usually negligible and it may often be assumed that the source is moving rapidly enough so that the irregularity motion may be ignored. Roughly speaking, the correlation time is the time taken for the penetration point at height h (Figure 33) to traverse a "typical" irregularity scale size. In general, a mixture of scale sizes are present, but the scale size most effective in producing amplitude scintillation has a radius of one Fresnel zone, i.e., $\sqrt{\lambda z}$, where λ is the observing wavelength. Thus, in a first approximation, the correlation time τ for amplitude fluctuations may be taken as

$$\tau \approx \frac{\sqrt{\lambda z}}{|V_p|} \quad (30)$$

where the effective penetration point speed V_p is given by

$$V_p = \frac{z_1}{z_2} (z_1 + z_2) \left(\dot{E}^2 + \dot{T}^2 \right)^{\frac{1}{2}} \quad (31)$$

\dot{E} and \dot{T} are the rates of change of elevation and traverse angle (traverse = azimuth x cosine of elevation), respectively, expressed in radians/sec.

In some circumstances the target may be moving such that V_p is small and the correlation times are determined by the motion of the irregularities. This is allowed for by adopting a minimum value of 100 m/sec for V_p , corresponding to a most probable irregularity speed.

J. Model for Angle Fluctuation

The UHF observations at Millstone Hill showed that angle scintillation was generally much more pronounced in traverse angle than in elevation angle. This is presumably related to the high inclination angle of the earth's magnetic field and the fact that the irregularities are elongated in the direction of the field.

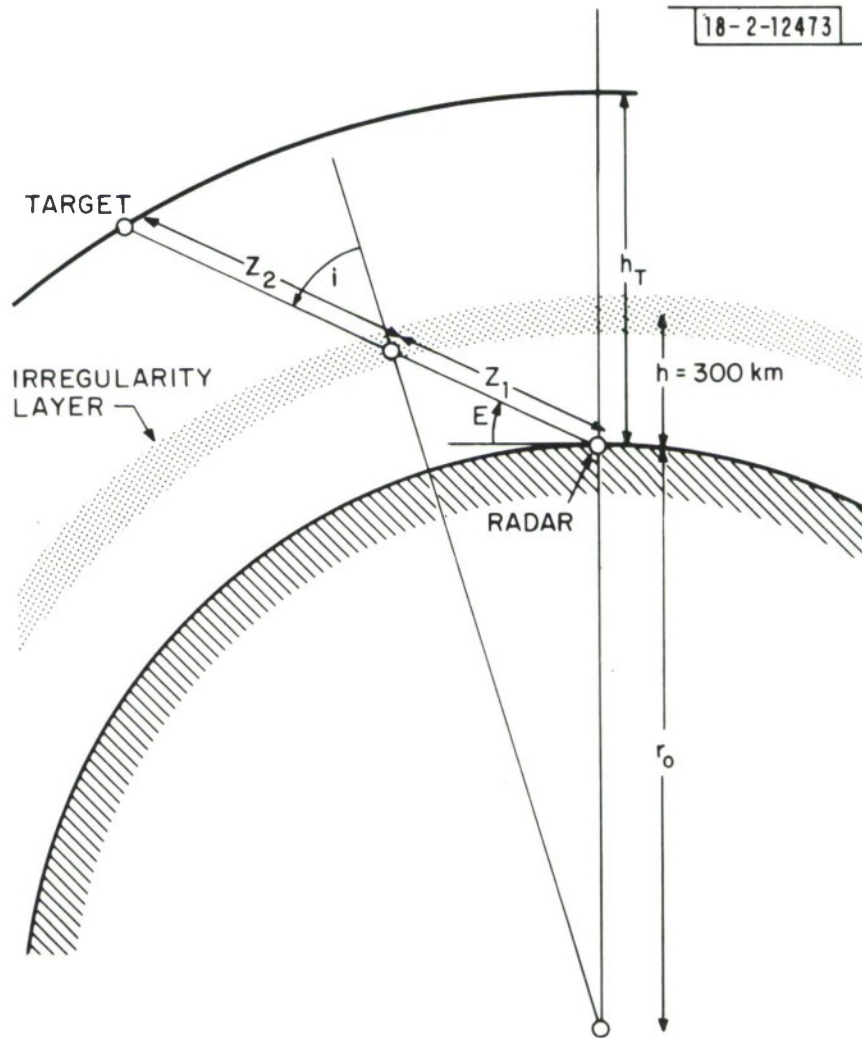


Fig. 33 Geometry for satellite tracking experiments.

The rms fluctuation in traverse angle about the mean over a three-second interval (σ_{TR}) was used to measure angle scintillation and the Millstone Hill study served to establish some relationships between the σ_{TR} and the amplitude scintillation index S at UHF. Figure 34 shows σ_{TR} v S during a period of intense scintillation occurring in a magnetic storm. It can be seen that the mean rms angular scintillation increases with S, but the two are not uniquely related. Whereas S is necessarily limited to a saturation value near unity, the angle fluctuations apparently continue to increase as the irregularities grow more intense.

The relationship between σ_{TR} and S using all satellite tracks is shown in Figure 35. In this analysis, the scintillation index was divided into a number of ranges and for each range the distribution of σ_{TR} values was constructed. The mean and most probable value for each distribution were calculated and are given in Figure 35.

The scintillation model for tracking simulation studies described above may be extended to cover traverse angle fluctuations by using the model value of S obtained from equation 22 to predict a model value of σ_{TR} from Figure 35. Before this procedure is satisfactory some thought must be given as to how the results in Figure 35 may be generalized to all frequencies rather than just the observing frequency of 400 MHz.

The frequency scaling law for angle scintillation needs to be established before any of the Millstone Hill observations made at 400 MHz can be used to estimate effects at higher frequencies. A detailed analysis of the spectra of the amplitude fluctuations observed at Millstone⁷ has shown that the irregularities in the ionosphere that are responsible have a power-law scale-size distribution with an index of four for the three-dimensional wave number spectrum. Theoretical analysis of the propagation of radio waves through a physically thick screen containing such irregularities has shown that for weak scattering the scintillation index (S) will scale with frequency (f) as $f^{-2/3}$, while the rms angle fluctuations scale as f^{-2} . Evidently, at higher frequencies the angle fluctuations will rapidly become insignificant even when amplitude fluctuations can be detected.

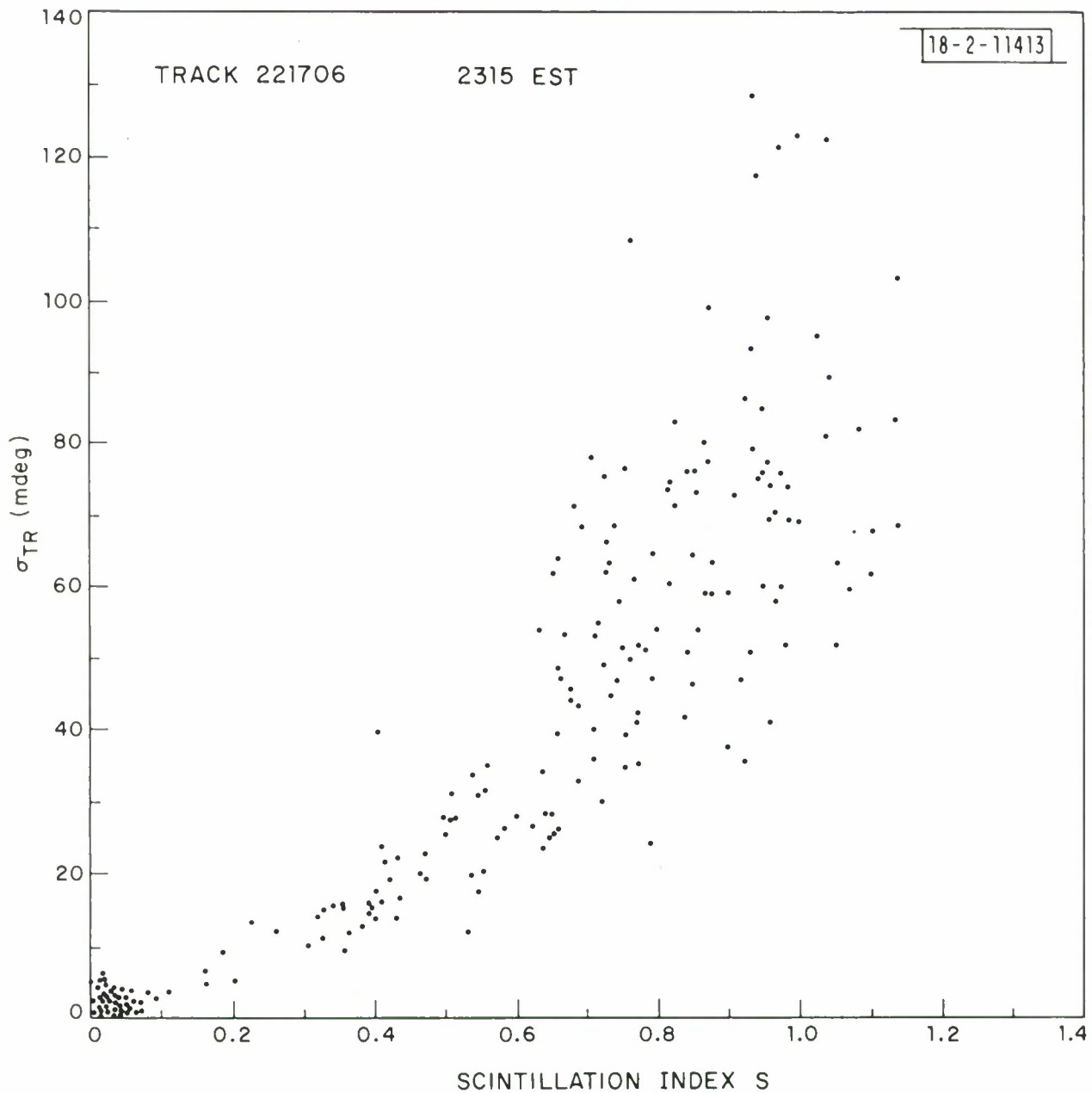


Fig. 34 RMS angular wander of target position in traverse at UHF vs the amplitude scintillation index S observed during a magnetic storm.

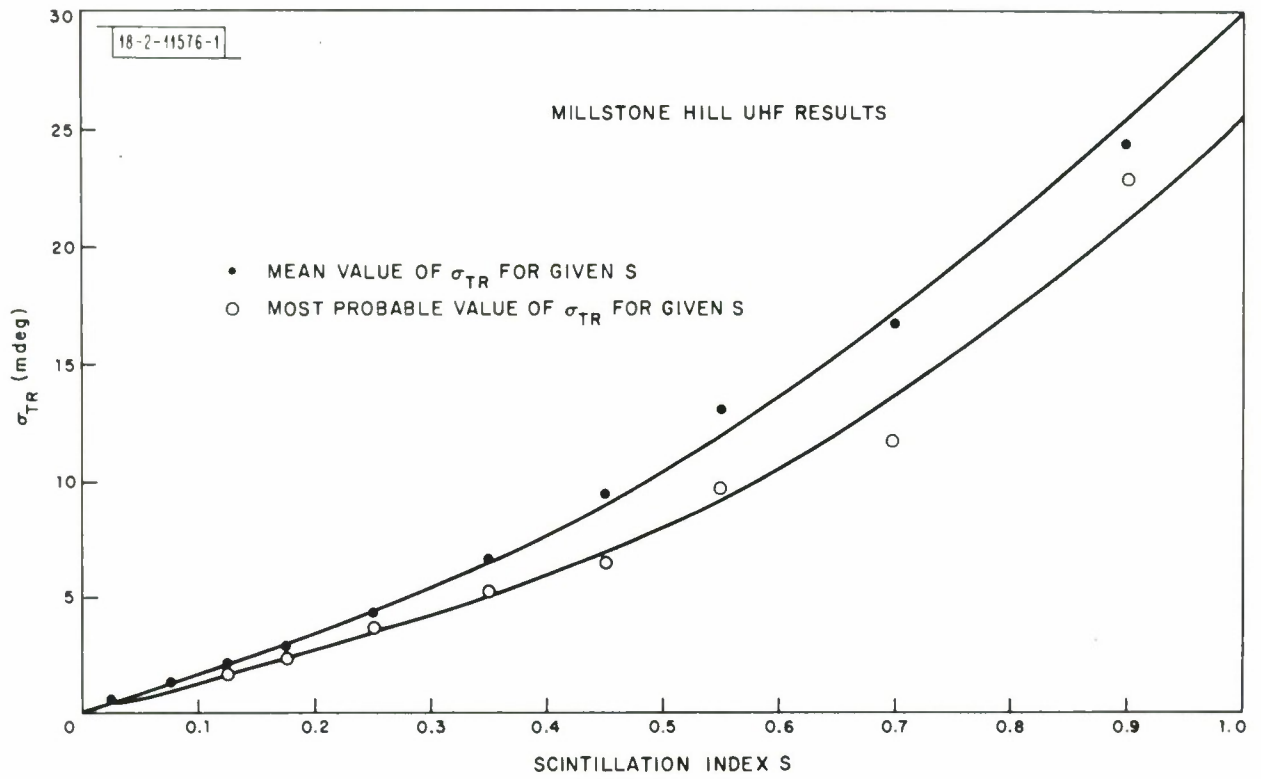


Fig. 35 The mean and most probable values of σ_{TR} as a function of scintillation index from UHF satellite beacon tracking records gathered at Millstone Hill from January 1971 to March 1973.

As there is an approximate linear relationship between σ_{TR} and S for $S < .5$ the frequency scaling laws suggest that this portion of the Figure 35 can be generalized for any frequency (f in MHz) of observation by adopting $\sigma_{TR} \left(\frac{400}{f}\right)^{\frac{1}{2}}$ as the ordinate rather than σ_{TR} . For larger values of S saturation effects are evident and in any case the frequency scaling laws become uncertain because the quoted relationships are only applicable for weak scatter. In view of these uncertainties the best approach is probably to assume that the figure as a whole can be applied at any frequency by using $\sigma_{TR} \left(\frac{400}{f}\right)^{\frac{1}{2}}$ as an ordinate rather than σ_{TR} .

The probability distribution of traverse angle fluctuations may be taken as Gaussian, while the correlation time may be assumed to be the same as for amplitude fluctuations (equation 30). No adjustment to the traverse angle fluctuation is necessary to allow for the two-way path involved in a radar situation.

K. Model for Severe Ionospheric Scintillation

A crude model of severe scintillation effects has been constructed to specify the upper limit to the magnitude of the fluctuations that might be expected for a radar operating at L-band (1000 MHz). The maximum degradation of radar performance caused by ionospheric scintillation can be determined by using this model in tracking simulation exercises. During geomagnetically disturbed conditions the probability of occurrence and intensity of scintillation increases markedly and a "worse-case model" was based on UHF measurements made at Millstone Hill at a period of severe magnetic disturbance ($K_p = 8+$). During this time the rms traverse angle fluctuation reached the largest value observed during the $2\frac{1}{2}$ years of the Millstone satellite tracking program, namely, 120 mdeg (Figure 34). The scintillation index at UHF reached the saturation level near unity and thus could not be used directly as a basis for extrapolation to L-band. The traverse angle rms did not exhibit any apparent saturation effects and scaling was accomplished by assuming the f^{-2} scaling law for angle fluctuations, giving an estimate of $\sigma_{TR} \approx 20$ mdeg at L-band (1000 MHz). Although this scaling law is supported both theoretically and experimentally under conditions of weak

scintillation, its use in the present case must be considered as a reasonable guess only. Using the curve in Figure 35 which relates the mean value of σ_{TR} to S, and an ordinate value of $\sigma_{TR} \left(\frac{400}{f} \right)^{\frac{1}{2}} = 13$ mdeg, provides an estimate of $S = 0.55$ for the worse-case model at L-band.

L. Summary of Scintillation Model

1. Amplitude Scintillation

A mean scintillation index \bar{S} (Λ) as a function of invariant latitude is obtained from the appropriate one of Figures 30a to 30f. The scintillation index for the observing frequency and target location is then estimated from equation 22 and converted to a rms amplitude fluctuation σ_R using equation 26. For the worse-case model at $f = 1000$ MHz a model value of $\sigma_R = .27$ is adopted independent of target location, provided it is above the irregularities. Based on σ_R , a value of the fluctuation in relative amplitude R for a one-way transmission is selected from a distribution of the form given by equation 27, with $m = (2 \sigma_R)^{-2}$. The actual radar amplitude is then obtained using equation 29. The correlation time may be calculated from equations 30 and 31, using the values of \dot{E} and \dot{T} for the track. The radar amplitude should be held constant for a time τ before selecting a new value from the model.

2. Angle Scintillation

The rms fluctuation in traverse angle σ_{TR} is calculated from the model value of S through Figure 35. For the worse-case model at $f = 1000$ MHz, σ_{TR} is taken as 20 mdeg. The actual traverse angle fluctuation is selected from a Gaussian distribution with zero mean and standard deviation σ_{TR} . This value should be held for a time τ , as for the amplitude.

M. Depolarization

A powerful discriminate against false targets is based on the depolarization of circularly polarized signals. There is concern that, during disturbed conditions, the auroral ionosphere could introduce sufficient depolarization to render this discriminate useless. This possibility was tested by R. Crane by analyzing the UHF beacon tracking results obtained in the Millstone Hill propagation study (Section II).

In many cases these signals exhibited severe angular and amplitude scintillation along paths at elevations below about 20-30° to the north of Millstone. Simultaneous observations of both left- and right-hand circular polarizations were recorded. (The transmissions were nominally right-hand circular, but proved in practice to be elliptically polarized.) The polarization state changed slowly with changes in satellite/receiver-station geometry. The gain of the orthogonal polarization receiver was controlled by the primary polarization AGC signal. The AGC control system was effective in removing fluctuations of limited dynamic range that occurred simultaneously on both channels at frequencies up to 250 Hz. For strong fluctuations with peak-to-peak spreads of more than 20 dB, the AGC system did not remove all of the simultaneous fluctuations from the orthogonal channel output, and residual fluctuations could be detected. For weak scintillation, only fluctuations on the orthogonal channel which were not correlated with the principal polarization fluctuations would be detected.

The August 1972 records for the most disturbed tracks observed during the three-year period, March 1970 - March 1973, were analyzed to measure the correlation between the right- and left-hand circular components. Figure 36 shows the rms log of the received power at 150 MHz and 400 MHz for the principal channel during a pass near 0400 hours GMT on 4 August 1972. It can be seen that at six minutes the UHF signal scintillation became fully developed.

The rms variation of the log of the orthogonal channel amplitude and the correlation coefficient between the log of the orthogonal channel output and the log of the principal channel output is shown in Figure 37 for the entire pass. For weak scintillation, (i.e., before six minutes) the output is near receiver noise and no correlation is evident. After seven minutes, the scintillation is much stronger and a low level variation is evident in the orthogonal channel data. However, this residual output is highly correlated with the scintillation in the principal polarization channel. The data, therefore, show no uncorrelated fluctuations.

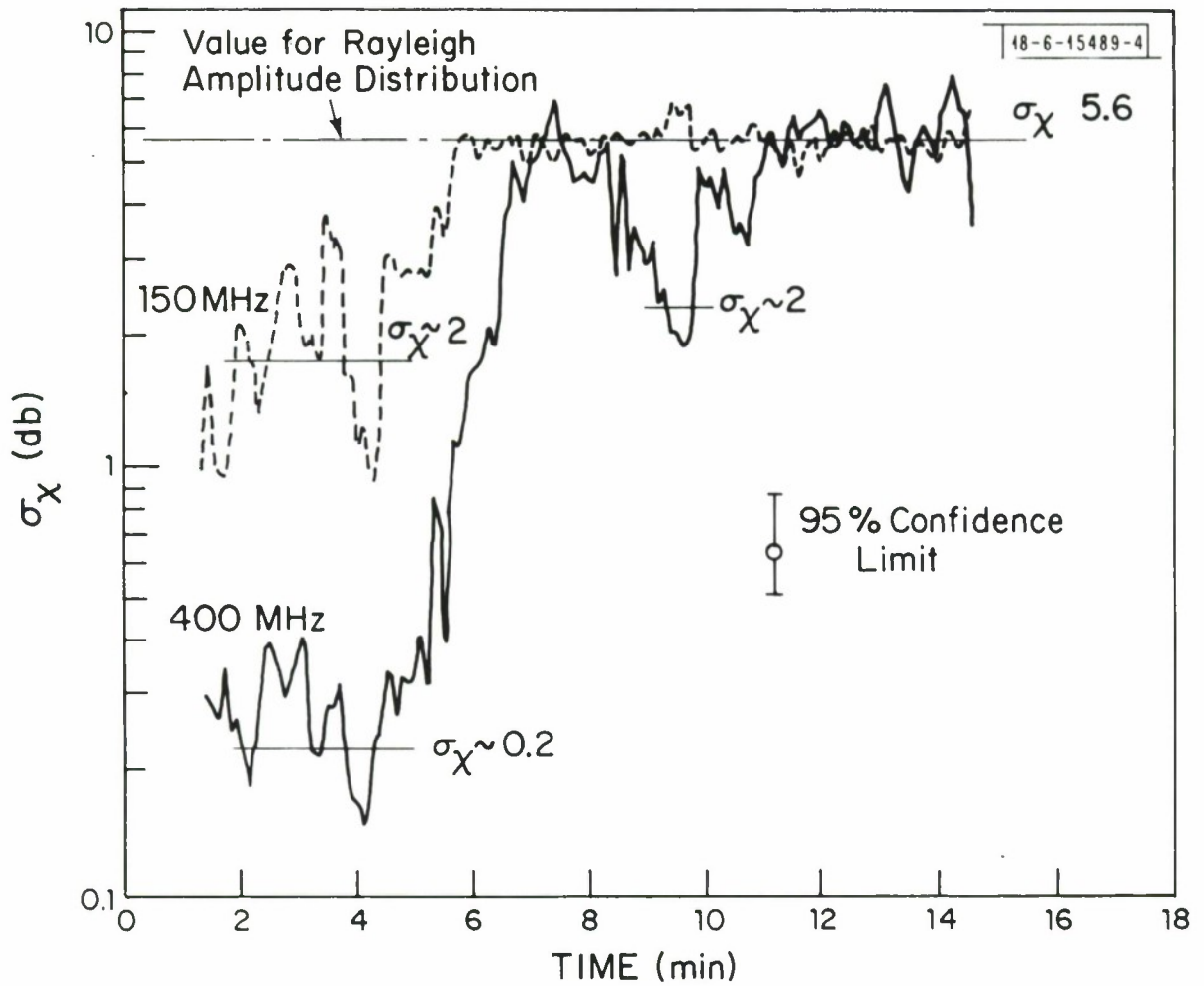


Fig. 36 RMS log (signal) vs time at 150 and 400 MHz for a very disturbed satellite pass in August 1972. It can be seen that the 150 MHz signal amplitude scintillation becomes completely developed before that at UHF.

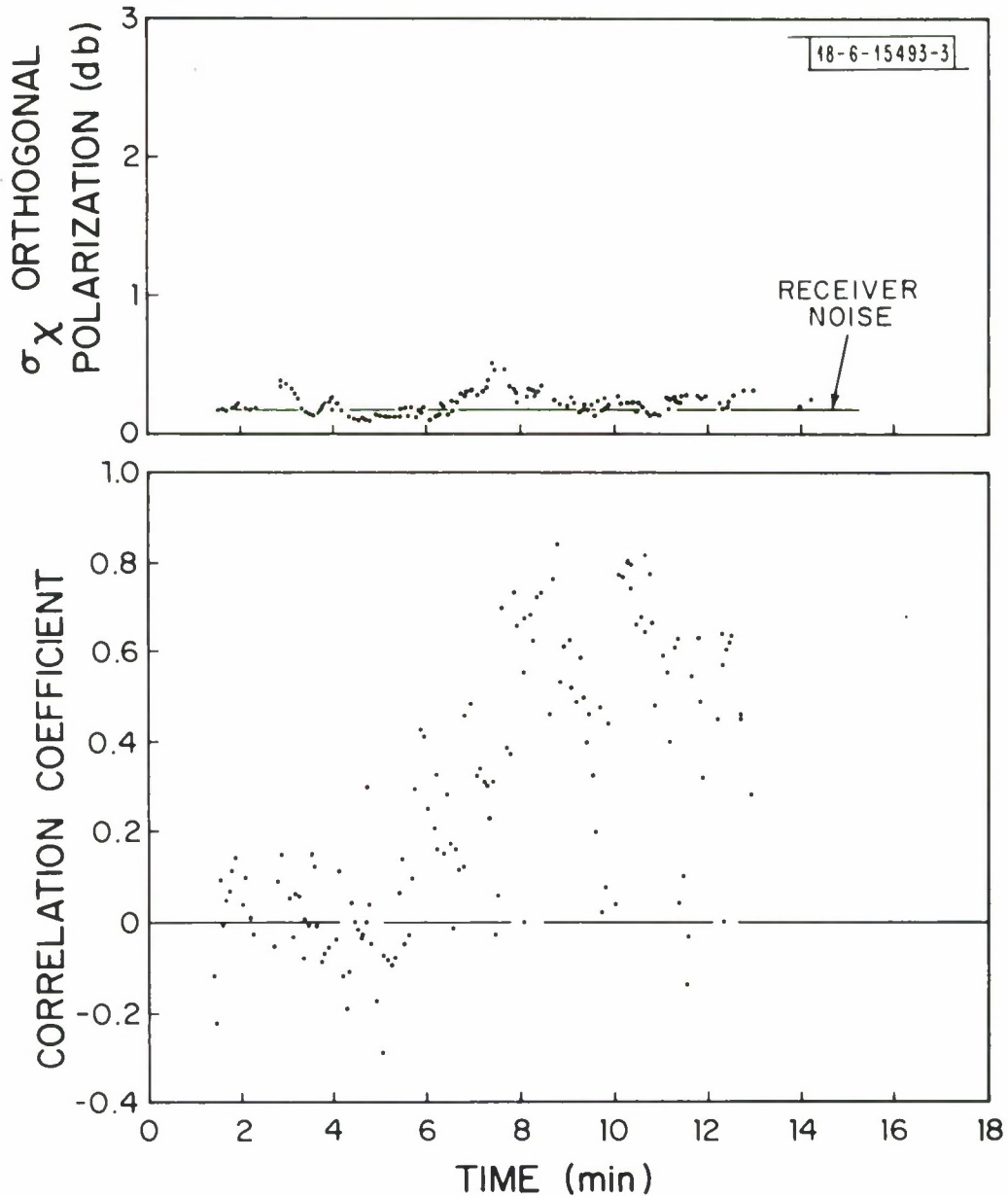


Fig. 37 RMS log (signal) vs time of the orthogonally polarized signal component and the correlation coefficient between the fluctuations at VHF and UHF, for the pass shown in Figure 36. At low scintillation and AGC circuit removes the fluctuations, but fails to do so for strong scintillation. Fades at both polarizations are found to be highly correlated.

These observations show that the fluctuations for both polarizations are correlated, i.e., both polarizations fade together. Thus, though the fading itself may be a nuisance, discrimination algorithms that depend upon observations of the depolarization of circularly polarized waves will not be affected adversely.

VIII. SUMMARY

Table 1 attempts to summarize the maximum values of the radar metric errors discussed above that are liable to be encountered at 1000 MHz at low elevations at a location near the auroral zone. It should be understood that the errors will generally be less than given here as the reported values in most cases were obtained from the worse cases observed over the duration of the Millstone Hill propagation study.

In particular, the scintillation result represents conditions during a severe magnetic storm and there must be some doubt as to the appropriate frequency scaling laws when such strong scintillation was present at UHF.

TABLE I

<u>SOURCE OF ERROR</u>	<u>MAXIMUM ERROR</u>	<u>FREQUENCY DEPENDENCE</u>
<u>Effects in the Ambient Ionosphere</u>		
Elevation Bias	+ 7 mdeg	f ⁻²
Range Bias	+ 75 m	f ⁻²
<u>Trough Effects</u>		
Elevation Error	+ 9 mdeg	f ⁻²
Range Error	- 10 m	f ⁻²
<u>TIDs</u>		
<u>λ > 100 km</u>		
Elevation Error (peak-to-peak)	10 mdeg	f ⁻²
Range Error (peak-to-peak)	5 m	f ⁻²
<u>λ < 100 km</u>		
Elevation Error (peak-to-peak)	10 mdeg	f ⁻²
<u>Scintillation</u>		
Relative amplitude (rms)	0.3	f ^{-3/2}
Azimuth (rms)	20 mdeg	f ⁻²

REFERENCES

1. J. V. Evans, Editor, "Millstone Hill Radar Propagation Study: Scientific Results", Lincoln Laboratory, MIT Tech. Rep. 509 (1973), Part I, DDC AD-781179/7; Part II, DDC AD-782748/8; Part III, DDC AD-780519/5.
2. B. H. Briggs and I. A. Parkin, "On the Variation of Radio Star and Satellite Scintillation with Zenith Angle", *J. Atmos. Terr. Phys.*, 25, 339-366 (1963).
3. J. V. Evans and J. M. Holt, "The Combined Use of Satellite Differential Doppler and Ground-Based Measurements for Ionospheric Studies", *IEEE Trans., Antennas Propag.* AP-21, 685-692 (1973), DDC AD-772225/9.
4. D. C. Badura, "Simulation of Electromagnetic Wave Propagation by Ray-Tracing Methods and Applications", Bell Telephone Laboratories, Whippany, N.J., Technical Report (in press 1975).
5. P. Leving, G. Millman, and B. Ostergaard, "Propagation Model for Errors Induced by Tropospheric and Ionospheric Refraction and Scintillation", Tech. Memo. TM-456-9018, General Electric, Syracuse, N.Y. (1973).
6. M. J. Rycroft and J. O. Thomas, "The Magnetospheric Plasmapause and the Electron Density Trough at the Alouette I Orbit", *Planet. Space Sci.*, 18, 65-80 (1970).
7. R. K. Crane, "Morphology of Ionospheric Scintillation", Lincoln Laboratory, MIT Tech. Note 1974-29 (21 May 1974), DDC AD-780522/9.
8. J. Aarons and R. S. Allen, "Scintillation Boundary during Quiet and Disturbed Conditions", *J. Geophys. Res.*, 76, 170 (1971).
9. J. Aarons, J. P. Mullen, and H. E. Whitney, "The Scintillation Boundary", *J. Geophys. Res.*, 74, 884-889 (1969).
10. J. V. Evans, Editor, "Millstone Hill Facility Monthly Report, 20 February 1974 to 19 March 1974", private communication.

REPORT DOCUMENTATION PAGE		READ INSTRUCTIONS BEFORE COMPLETING FORM
1. REPORT NUMBER ESD-TR-75-175	2. GOVT ACCESSION NO.	3. RECIPIENT'S CATALOG NUMBER
4. TITLE (and Subtitle) Ionospheric Limitations on Radar Accuracy at L-Band		5. TYPE OF REPORT & PERIOD COVERED Technical Note
		6. PERFORMING ORG. REPORT NUMBER Technical Note 1975-28
7. AUTHOR(s) Wand, Ronald H.		8. CONTRACT OR GRANT NUMBER(s) F19628-73-C-0002
9. PERFORMING ORGANIZATION NAME AND ADDRESS Lincoln Laboratory, M.I.T. P.O. Box 73 Lexington, MA 02173		10. PROGRAM ELEMENT, PROJECT, TASK AREA & WORK UNIT NUMBERS Project No. 8X363304D215
11. CONTROLLING OFFICE NAME AND ADDRESS Ballistic Missile Defense Program Office Department of the Army 1320 Wilson Boulevard Arlington, VA 22209		12. REPORT DATE 27 May 1975
		13. NUMBER OF PAGES 84
14. MONITORING AGENCY NAME & ADDRESS (if different from Controlling Office) Electronic Systems Division Hanscom AFB Bedford, MA 01731		15. SECURITY CLASS. (of this report) Unclassified
		15a. DECLASSIFICATION DOWNGRADING SCHEDULE
16. DISTRIBUTION STATEMENT (of this Report) Approved for public release; distribution unlimited.		
17. DISTRIBUTION STATEMENT (of the abstract entered in Block 20, if different from Report)		
18. SUPPLEMENTARY NOTES None		
19. KEY WORDS (Continue on reverse side if necessary and identify by block number) L-band radar ionospheric effects scintillation effects satellite tracking Millstone Hill		
20. ABSTRACT (Continue on reverse side if necessary and identify by block number) For a long-range radar system the target range and bearing, as well as the signal amplitude and phase, are altered to some degree by the presence of the earth's atmosphere and ionosphere. The irregular nature of the ionosphere controls the extent to which these errors can be predicted and compensated for. The limits on radar metric accuracy imposed by ionospheric propagation effects are evaluated with emphasis on an L-band radar situated near the auroral zone. Many of the results are derived from previous propagation studies conducted at the Millstone Hill radar facility by applying appropriate frequency scaling laws. Estimates are made of elevation and range errors associated with the ambient ionosphere and with large-scale ionospheric structures (such as the mid-latitude electron density trough and traveling ionospheric disturbances). The amplitude and angle-of-arrival fluctuations produced by ionospheric scintillation are considered and models constructed which are applicable for normal ionospheric conditions and also for periods of severe geomagnetic disturbance.		